



CENTRO DE INVESTIGACIONES
EN OPTICA, A.C.

**VERSION DEFINITIVA. INCLUYE CAMBIOS
SUGERIDOS POR LOS REVISORES**

**“INTEGRATED MICRORING RESONATORS FOR
PHOTONIC QUANTUM TECHNOLOGIES”**



Tesis que para obtener el grado de Doctor en Ciencias (Óptica)

Presenta: Juan Samuel Sebastián Durán Gómez

Director de Tesis: Dr. Roberto Ramírez Alarcón

Co – Director de Tesis: Dr. Rafael Salas Montiel

León · Guanajuato · México

Diciembre de 2024

To my parents: Alberto Duran and Cristina Gomez, this achievement is deserved thanks to both of you. The advice, effort and encouragement that you gave me through all these years is now reflected in this document.

Acknowledgements

I would like to express my sincere gratitude to those who have helped and supported me over the last four years.

Firstly, I am deeply grateful to my parents, Alberto Durán and Cristina Gómez, my siblings, Sergio, Eduardo, Valeria, and Daniela, as well as to my partner, Anabel, and my two children, Emily and Christian. This achievement belongs to them for all their time, support, and patience throughout this journey. All of you have been incredibly important to me throughout my career, and I am deeply indebted to each of you.

Mom and Dad, you are my heroes, and I am so grateful to have you as parents. I will always remember the sacrifices you made to help our family grow and improve our quality of life.

Anabel, thank you for trusting in me. You have been so supportive, and I am grateful for all the ways you've supported our family.

Lalito, you are one of my best friends for life. I truly appreciate your support when I am away from home. I must say, thank you, brother.

Emily and Christian, my little ones, I am sorry for the time I have spent away from you. I truly hope this sacrifice will bring us better opportunities.

To all my family, may your lives be blessed.

I am grateful to my advisors. I would like to thank Prof. Roberto Ramirez Alarcón for allowing me to work with him. I appreciate his guidance, support, and dedication, as well as his talks and advice, which were always so timely and helped me grow in every way, especially in my professional development and in personal matters. Thank you, Roberto. You are not only an excellent advisor but also a great friend.

Furthermore, I would like to thank Prof. Rafael Salas-Montiel for accepting the co-direction and for his support throughout the entire doctoral program. Thank you,

Rafa. Your guidance, teaching, and support have been invaluable to me.

Moreover, I would like to acknowledge Prof. Michael Kues for his support, teaching, advice, and for the trust he has shown me since we first met, as well as for accepting the internship and providing the equipment for the measurements and results presented in this thesis. Thank you, Michael, for your trust, advice, and support.

I would like to express my gratitude to my doctoral committee for supporting and enriching my work to improve it: Dr. Laura Rosales, Dr. Verónica Vázquez, and Dr. Alfredo Benítez. Additionally, I would like to express my gratitude to my examiners, Dr. Laura Rosales, Dr. Verónica Vázquez, and Dr. Lorena Velázquez, for taking the time to evaluate my research.

I would like to thank my tutor, Dr. Laura Rosales. Your trust, support, and advice have been very helpful in my personal and professional life.

I am grateful to my friends at CIO for the knowledge, time, and experiences shared during my PhD: Gerardo, Edwin, Guillermo, Dante, and Alex. I will always remember the special conversations and the good moments we shared, as well as the times we enjoyed drinking great coffee together. I must say, you are my best friends.

Furthermore, I would like to thank my colleagues and friends from the Institute of Optical Technologies in Hannover: Ali, Jan, Philip, Robert, Hatam, Rajh, and Muhamed. Special thanks to Ali Angulo, Jan Heine and Philip Rübeling for the knowledge and collaboration provided during my internship. Thank you all for sharing your time with me and for enjoying a cup of coffee together. Special acknowledgments to Jan Heine, the measurements corresponding to the sample 2 were performed by him.

Finally, I would like to express my gratitude to the CONAHCYT scholarship program for providing me with financial support over the past four years.

Declaration of authenticity

I hereby declare that this work is constituted by my authorship, except when specific reference is made to the work of other people. The content of this thesis is original and has not been fully or partially presented for any other degree in this or any other study center. This thesis is the result of my own work and does not include anything that is the result of any work done in collaboration, unless specifically indicated in the text.

Juan Samuel S. Durán Gómez.
León, Guanajuato, México.
November 2024.

Abstract

Photonic quantum technology is an emerging field that combines integrated photonics with the principles of quantum mechanics to manipulate and control photonic quantum states for applications such as computing, communication, and sensing. These technologies exploit quantum phenomena, such as superposition, entanglement, and quantum interference, to perform tasks that are impossible or inefficient using classical systems. Moreover, photonic quantum devices require three main stages for their full implementation: generation, manipulation, and detection of quantum states of light.

In this work, we focus on the generation of quantum states of light by engineering integrated photon sources that exploit the Spontaneous Four Wave Mixing (SFWM) process. We describe the theoretical background and the detailed process for designing two different integrated photon sources based on microring resonators in a Si_3N_4 platform for various applications:

- The first integrated photon source consists of an integrated microring resonator that is capable of producing photons that are wide-spectrally separated where one of these photons is centered at $\lambda_s = 606$ nm, corresponding to the atomic transition of a quantum memory based on $\text{Pr}^{3+}:\text{Y}_2\text{SiO}_5$ crystal, while the idler photon is centered at ITU channel 43 for its distribution in a fiber network. In addition, we determine the minimal Q-factor of the cavity required to achieve the 4 MHz bandwidth to match the spectral properties of the Pr ions.
- The second integrated photon source consist of a simple microring resonator with a single bus waveguide coupled to it, designed to produce a broadband spectrum. This is achieved by engineering the dispersion profile with different widths for a fixed height. We compare our proposed geometry in terms of photon flux and bandwidth generation with recently reported geometries used in the Si_3N_4 platform.

Overall, in the process of designing these two integrated photon sources, we explore and engineer the dispersion parameters to tailor the photon source to a specific application,

considering the width in the fabrication process as the only degree of freedom.

Additionally, we characterize the integrated microring resonator tailored for broadband frequency comb generation, which was fabricated at UTT in France. The transmission spectrum is measured for both TE and TM polarizations supported by the microring resonators, which allows us to corroborate theoretical key parameters of the resonators, such as the Free Spectral Range (FSR) and integrated dispersion. Furthermore, we characterize the Q-factor of these resonators for several gap sizes using a Lorentzian fit and estimate the bandwidth of the resonances. This characterization is the first step in deploying our proposed integrated photon sources, which, once the fabrication process is improved, will allow us to proceed with the generation of frequency-correlated photons.

Contents

List of Figures	xiii
List of Tables	xvii
1 Introduction	1
1.1 Overview, motivation, and challenges	1
1.2 Scientific objectives	3
1.2.1 Specific objectives	3
1.3 Scope and outline of the thesis	4
2 Theoretical background	5
2.1 Introduction	5
2.2 Maxwell's equations in dielectric media	5
2.2.1 Electromagnetism as an eigenvalue problem	7
2.2.1.1 Fundamental properties of eigenmodes	7
2.2.2 Numerical methods: WMM mode solver and eigenmode expansion	7
2.2.2.1 WMM Mode Solver	8
2.2.3 Group refractive index	9
2.2.4 Dispersion	9
2.2.5 Integrated microring resonators	9
2.3 Nonlinear processes	12
2.3.1 Spontaneous Four Wave Mixing	12
2.3.2 Joint Spectral Intensity of SFWM	13
2.4 Conclusion	15
3 Photon Source for a Quantum Memory	17
3.1 Introduction	17
3.2 Design of the integrated photon source	18
3.3 Effective refractive index and dispersion	20
3.4 SFWM phase-matching condition	22
3.4.1 Phase-matching for the TM mode	22
3.4.2 Phase-matching for the TE mode	24
3.5 Integrated dispersion and frequency mismatch	25

CONTENTS

3.6	Two-photon quantum state of the cavity	28
3.7	Bandwidth determination of the photon source	30
3.8	Photon pair generation estimation	31
3.9	Conclusion	32
4	Broadband Frequency Comb Generation by Dispersion Engineering	33
4.1	Introduction	33
4.2	Simulation of a broadband integrated photon source	34
4.2.1	Dispersion comparison for silicon dioxide and air cladding	34
4.2.2	SFWM phase-matching condition	38
4.2.3	Cavity effect in the SFWM process	41
4.2.4	Frequency comb and flux of photons	43
4.3	Fabrication and characterization of integrated microring resonators.	45
4.3.1	GDSII file	46
4.3.2	Transmission spectra measurements	47
4.3.3	Sample 1	48
4.3.3.1	TE polarization	48
4.3.3.2	Temperature shifting for the TE mode	50
4.3.3.3	TM polarization	51
4.3.4	Sample 2	53
4.4	Conclusion	56
5	Conclusions	57
5.1	Perspectives	59
	List of Publications	61
	Bibliography	63

List of Figures

2.1	Cross section of the optical waveguide used for our simulations.	8
2.2	Schematic representation of a microring resonator coupled to a bus waveguide.	10
2.3	Schematic representation of the SFWM, two photons from a pump are annihilated to create a signal and idler photon pair.	13
3.1	a) Schematic representation of an integrated photon source based on SFWM using a microring resonator that produces photon pairs capable of interacting with a $\text{Pr}^{3+}:\text{Y}_2\text{SiO}_5$ solid state quantum memory, and b) scheme of energy levels of $\text{Pr}^{3+}:\text{Y}_2\text{SiO}_5$ crystal.	19
3.2	Cross section of a Si_3N_4 on insulator ridge waveguide with air cladding.	20
3.3	Effective refractive index as a function of the wavelength for different widths and a fixed height of $h = 430$ nm for the TE_{00} (solid line) and TM_{00} (dashed line) modes. Si_3N_4 and SiO_2 bulk refractive indices are used to delimit the guided modes ($n_{eff} > n_{\text{SiO}_2}$).	21
3.4	Dispersion parameter for TE_{00} and TM_{00} modes. The gray zone delimits the anomalous dispersion $D_\lambda > 0$ for a waveguide with $w = 818$ nm and $h = 430$ nm considering the TE_{00} mode.	22
3.5	Contour plots of the phase-matching condition in terms of the detuning frequency $\Omega_{s,i}$ for the TM_{00} mode i.e., $\Delta\beta(\omega) = 0$	23
3.6	Wavelength of the signal and idler photons as a function of the pump wavelength for the TM_{00} mode.	23
3.7	Contour plots of the phase-matching condition in terms of the detuning frequency $\Omega_{s,i}$ for the TE_{00} mode i.e., $\Delta\beta(\omega_p) = 0$	24
3.8	Wavelength of the signal and idler photons as a function of the pump wavelength for the TE_{00} mode.	25
3.9	Integrated dispersion as a function of the frequency when the pump frequency is centered at $\nu_p = 352.139$ THz.	26
3.10	Normalized resonances for the three different radii and for the pump, signal and idler photons, respectively, centered at the optimal frequencies.	27
3.11	Frequency mismatch for three different ring radii where the minimal frequency mismatch is obtained at the optimal ring radius.	28

LIST OF FIGURES

3.12	Simulation of the JSI for the two-photon quantum state generated by the proposed microring resonator in the (ν_s, ν_i) space for one nonoptimal radius ($R_1 = 152.814 \mu\text{m}$). a) JSI calculated in the cavity absence, b) cavity effect obtained by the resonator and c) resulting cavity-enhanced JSI.	29
3.13	Simulation of the JSI for the two-photon quantum state generated by the proposed microring resonator in the (ν_s, ν_i) space for the optimal radius ($R_2 = 155.255 \mu\text{m}$). a) JSI calculated in the cavity absence, b) cavity effect obtained by the resonator and c) resulting cavity-enhanced JSI.	29
3.14	Simulation of the JSI for the two-photon quantum state generated by the proposed microring resonator in the (ν_s, ν_i) space for one nonoptimal radius ($R_3 = 159.989 \mu\text{m}$). a) JSI calculated in the cavity absence, b) cavity effect obtained by the resonator and c) resulting cavity-enhanced JSI.	29
3.15	Normalized marginal functions obtained by integrating the JSI a) over the idler frequency ν_i and b) over the signal frequency ν_s . The spectral bandwidth is obtained at the FWHM giving a value of $\Delta\nu_{s,i} = 3.98 \text{ MHz}$ for both photons.	30
3.16	Norm of the electric field distribution of the TE_{00} mode for the a) signal ($\lambda_s = 606 \text{ nm}$), b) pump ($\lambda_p = 851.347 \text{ nm}$) and c) idler ($\lambda_i = 1430.5 \text{ nm}$) photons.	31
4.1	Schematic representation of a frequency comb generated by a single bus microring resonator photon source.	33
4.2	Cross section of a Si_3N_4 on insulator ridge waveguide with: a) air cladding and b) SiO_2 cladding.	35
4.3	Dispersion as a function of the wavelength for a fixed height $h = 500 \text{ nm}$, considering SiO_2 and air cladding for several widths for: a) the TE_{00} mode and b) TM_{00} mode.	36
4.4	Dispersion as a function of the wavelength for two cases: thickness of 500 nm (air cladding) and 800 nm (SiO_2 cladding) for three different widths each one and for: a) the TE_{00} mode and b) TM_{00} mode.	37
4.5	Contour plots of the phase-matching condition in terms of the detuning frequency $\Omega_{s,i}$ i.e., $\Delta\beta(\omega) = 0$, for two cases: thickness of 500 nm (air cladding) and 800 nm (SiO_2 cladding) for three different widths each one and for: a) the TE_{00} mode and b) TM_{00} mode.	38
4.6	Wavelength of the signal and idler photons as a function of the pump wavelength for two cases: thickness of 500 nm (air cladding) and 800 nm (SiO_2 cladding) for three different widths each one and for: a) the TE_{00} mode and b) TM_{00} mode.	39

4.7	Phase-matching a function of the wavelength in a waveguide with 1 cm length and for two cases: thickness of 500 nm (air cladding) and 800 nm (SiO ₂ cladding) for three different widths each one and for: a) the TE ₀₀ mode and b) TM ₀₀ mode.	40
4.8	Cavity function $\mathcal{M}_{cav}(\nu_s, \nu_i)$ where it is clearly visible how the resonances become narrower when increasing the Q-factor for a) $Q = 10^4$, b) $Q = 10^5$ and c) $Q = 10^6$	41
4.9	Norm of the electric field distribution of the TE ₀₀ mode with the respective effective area for a) 1300 nm width and 500 nm height and b) 1700 nm width and 800 nm height.	42
4.10	Simulation of the normalized Joint Spectral Intensity for the two different configurations of ring resonators. a) Frequency comb generated by the ring with width 1300 nm and 500 nm height, and b) frequency comb generated by the ring with width 1700 nm and 800 nm height.	43
4.11	Simulated flux of photons for the correlated modes for the two different configurations of ring resonators.	44
4.12	Schematic representation of the full process of electron beam lithography for the nanofabrication of nanostructures: a) The sample with a thin film of Si ₃ N ₄ , b) deposition of the e-beam resist with spin coating technique, c) pattern exposure to the electron beam, d) development of the sample to remove the exposed resist and e) reactive ion etching process for the transfer of the pattern to the Si ₃ N ₄ thin film.	45
4.13	GDSII designs of the integrated photon source. The three different rings with the three different gaps are shown.	46
4.14	Microscope images of the first sample of ring resonators.	47
4.15	Schematic representation of the setup used to characterize and measure the ring resonators.	47
4.16	Microscope images for the coupling and outcoupling of light in the micro ring resonator. a) Fiber lens used to couple light to the photonic chip and b) output of the chip in the Si ₃ N ₄ taper and the SU8 waveguide.	48
4.17	a) Normalized transmission spectra measured for different gaps of a ring resonator for the TE ₀₀ mode. Resonance dips for different gaps and fitted to a Lorentzian function extracting the bandwidth at FWHM, b) $g = 400$ nm with a bandwidth $\Delta\nu = 10.29$ GHz, c) $g = 600$ nm with a bandwidth $\Delta\nu = 6.04$ GHz and d) no resonance dip identified which shows the bus waveguide is not interacting with the resonator.	49
4.18	Integrated dispersion as a function of the frequency for the TE ₀₀ mode. The theoretical value of the integrated dispersion is shown as the black line, while the dots correspond to the peaks measured from the transmission spectra for all the rings of the sample 1.	50
4.19	Normalized transmission spectra measured for a ring resonator for the TE ₀₀ mode with different temperatures showing the shifting.	50

LIST OF FIGURES

4.20	Shifting of the peaks taken from the previous spectra and their corresponding fittings as a function of the temperature written in: a) frequency detuning and b) wavelength detuning.	51
4.21	a) Normalized transmission spectra measured for different gaps of a ring resonator for the TM_{00} mode. Resonance dips for different gaps and fitted to a Lorentzian function extracting the bandwidth at FWHM, b) $g = 400$ nm with a bandwidth $\Delta\nu = 14.38$ GHz, c) $g = 600$ nm with a bandwidth $\Delta\nu = 7.24$ GHz and d) $g = 600$ nm with a bandwidth $\Delta\nu = 5.92$ GHz.	52
4.22	Integrated dispersion as a function of the frequency for the TM_{00} mode. The theoretical value of the integrated dispersion is shown as the black dashed line, while the dots correspond to the peaks measured from the transmission spectra for all the rings of the sample 1.	53
4.23	a) Normalized transmission spectra measured for different gaps of a ring resonator for the TE_{00} mode. Resonance dips for different gaps and fitted to a Lorentzian function extracting the bandwidth at FWHM, b) $g = 350$ nm with a bandwidth $\Delta\nu = 8.02$ GHz, c) $g = 400$ nm with a bandwidth $\Delta\nu = 6.92$ GHz, d) $g = 450$ nm with a bandwidth $\Delta\nu = 5.68$ GHz and e) $g = 500$ nm with a bandwidth $\Delta\nu = 6.95$ GHz.	54
4.24	Integrated dispersion as a function of the frequency. The theoretical value of the integrated dispersion is shown as the black line, while the dots correspond to the peaks measured from the transmission spectra for all the rings of the sample 2.	55

List of Tables

3.1	Wavelengths of the pump, signal and idler, where the pump wavelength is determined by using equation 3.1.	19
3.2	Radius and wavelength of the resonances for the pump, signal and idler, where the resonances are determined by the resonance condition ($\beta L = 2\pi l$).	26
4.1	Summary of the parameters for the resonator considering the TE ₀₀ mode.	42
4.2	Summary of the measured parameters for both samples and different gaps in the microring resonators.	55

1.1 Overview, motivation, and challenges

Quantum technologies have been emerging in the last decades as a field of research that could provide advantages over classical systems, such technologies take advantage of the properties and phenomena encountered in quantum mechanics particularly, in quantum optics [1, 2].

Within this framework, integrated quantum photonics is a research field based on photonic circuit technology to generate, manipulate and control quantum states of light for a variety of applications, including quantum computing, communication, and sensing [3, 4, 5, 6, 7]. By integrating photonic components such as waveguides, detectors, and modulators on a single chip, it is possible to create compact, scalable, and highly efficient quantum systems [8, 9]. This integration enables the generation, processing, and detection of quantum information encoded in photons, offering significant advantages in terms of miniaturization, performance, and cost-effectiveness compared to traditional quantum bulky optical setups. As the field advances, integrated quantum photonics is a promising candidate for enabling practical quantum technologies with real-world applications [10, 11, 12, 13].

In this case, photons are regarded as the ideal carriers of information due to their high transmission speed, low decoherence, and minimal information loss. Quantum bits, or qubits, which can be represented by any physical two-level quantum system, can be encoded in the polarization state of photons and thus manipulated. Additionally, other degrees of freedom, such as path, can be used to encode quantum information [8, 9].

Hence, the generation of photonic quantum states constitutes a challenge in the efficient development of quantum technologies where photon sources are required. Correlated photon pair sources can be implemented through two well-known processes: Spontaneous Parametric Down Conversion (SPDC) and Spontaneous Four Wave Mixing (SFWM) [14, 15, 16]. SPDC is a second-order nonlinear process where, a nonlinear material is pumped in which one photon is annihilated to create a photon pair. Typi-

cally, this process is exploited using crystals in bulk setups. On the other hand, SFWM is a third-order nonlinear process where two photons are annihilated and create a photon pair; unlike SPDC, SFWM is implemented in fibers or waveguides. For both processes, the phase-matching and energy conservation are essential for an efficient generation of photons [14, 15, 16].

Following this idea, obtaining efficient integrated photon sources that exploit SFWM presents a challenge today. To achieve this, materials with strong nonlinear third-order susceptibility are being investigated, typically those with a high refractive index [5, 9, 12, 15, 17]. In consequence, the role of the fabrication process is fundamental.

It has been demonstrated that femtosecond (fs) laser writing allows for the fabrication of optical waveguides with sizes on the order of a few microns [3, 18, 19]. However, direct fs laser written waveguides are limited in size by the optical diffraction limit of the lenses. This limit can be overtaken with the use of the electron beam lithography writing technique [20, 21, 22]. Current advances in nanofabrication allow us to foresee the implementation of photonic quantum devices. In general, integrated photonics serve as an excellent platform for the generation, manipulation, and detection of photons [21, 22, 23, 24].

Moreover, Si_3N_4 is a novel material used in nanophotonic circuits due to its attractive optical properties, low propagation loss, and high compatibility with current CMOS technology. Si_3N_4 possesses a high refractive index in comparison with other materials, enabling efficient light confinement and guiding in optical waveguides. For instance, Si_3N_4 does not exhibit Two Photon Absorption (TPA) or Free Carrier Absorption (FCA), two processes present in Silicon On-Insulator (SOI) circuits that affects the performance of photonic chips. Furthermore, Si_3N_4 is of interest for its broad transparency window that covers from the visible to the near-infrared spectrum, making it suitable for a wide range of applications, including optical communication, sensing, and quantum photonics [5, 11, 17, 25].

In this PhD thesis, we focus on the design of integrated photon sources using integrated cavities in silicon nitride platform. We engineer the dispersion of the waveguides to tailor the spectral properties of the photon source considering the width and the radius of the cavity as the two degrees of freedom. Furthermore, we study the spectral properties of the photon source by analyzing the Joint Spectral Intensity (JSI).

In particular, we show the detailed process in the design of two photon sources with different potential applications. The first photon source is tailored to produce photons with a wide spectral separation where the signal photon must match the spectral properties of a quantum memory based on a $\text{Pr}^{3+}:\text{Y}_2\text{SiO}_5$ crystal, while the idler photon is compatible to match the center of an ITU channel of a Course Wavelength Division Multiplexing (CWDM) commercial system.

The second photon source is engineered to produce a broadband quantum frequency comb by using an air-cladding configuration which in combination with the microring resonator, enhances the photon flux in comparison with recent photon sources that use a SiO₂ cladding. Additionally, the proposed photon source can generate frequency-correlated photon pairs with a 50 GHz spacing and low dispersion, making it highly compatible with a 50 GHz grid Dense Wavelength Division Multiplexing (DWDM) system.

Although the objective of the thesis is the design and simulation of photon sources by the nonlinear process of SFWM, we additionally show a brief review on the fabrication process of one of these integrated photon sources and the classical characterization.

This work is developed within the framework of a collaboration between the *Université de Technologie de Troyes, France*, *Centro de Investigaciones en Óptica A.C., Mexico* and the *Leibniz Universität Hannover, Germany*. One of the specific goals of the collaboration is the fabrication, characterization and implementation of integrated photonic circuits for potential photonic quantum technologies.

1.2 Scientific objectives

Our primary objective is to design and fabricate integrated photon sources utilizing microring resonators for photonic quantum applications where the spectral properties of the photon sources are tailored by dispersion engineering, mainly, by changing the width of the optical waveguides.

To accomplish this goal, we established the following specific objectives:

1.2.1 Specific objectives

- To simulate optical waveguides and microring resonators in Si₃N₄ platform.
- To theoretically simulate the JSI for optimal conditions and determine their spectral properties through the use of integrated cavities such as wavelength and bandwidth of the generated photons.
- To fabricate the integrated photon sources with electron beam lithography and reactive ion etching processes.
- To characterize the photonic devices and corroborate the measurements with the theoretical model.

1.3 Scope and outline of the thesis

This thesis aims to provide the steps followed in the design of two particular integrated photon sources. First, an integrated photon source capable of producing photons for interacting with a solid state quantum memory. Second, an integrated photon source engineered to produce a broadband quantum frequency comb.

This thesis manuscript is divided into four chapters.

Chapter 2: We describe the theoretical formulation for optical waveguides, a brief review on quantum optics and nonlinear optics. Afterwards, we discuss the theoretical background of microring resonators and SFWM process.

Chapter 3: We describe the detailed procedure to design an integrated cavity that matches the spectral properties of praseodymium ions in a crystal ($\text{Pr}^{3+}:\text{Y}_2\text{SiO}_5$). The analysis begins by determining the geometrical parameters of the waveguide, such as width, height, and radius, to match the wavelength of the atomic transition of the Pr ions. Subsequently, we obtain the minimal quality factor to achieve the bandwidth of the photons which is the only limitation due to the high narrow bandwidth required.

Chapter 4: In this chapter, the design of an integrated photon source is detailed, that is capable of producing a broadband quantum frequency comb at telecom wavelengths. To achieve this, we compare air and SiO_2 as materials considered as claddings. Furthermore, we show the advantages of using an air-cladding, and we compare the photon flux expected from two photon sources: our proposed photon source with a thickness of 500 nm and air cladding and, recent experimental photon sources with thickness of 800 nm with SiO_2 cladding.

Chapter 5: Finally, we summarize the conclusions of the present work and discuss some interesting points regarding the development of these devices and future work.

Theoretical background

2.1 Introduction

This chapter introduces the theoretical fundamental concepts in optical waveguides and quantum optics that are relevant to this research work. It begins with the description of Maxwell's equation in dielectric media. The determination of the guided modes as well as the fundamental properties of the optical modes such as dispersion is also presented in this chapter.

We introduce the mathematical description for integrated optical cavities and the most important parameters. Furthermore, we describe the theoretical formulation of the Spontaneous Four Wave Mixing (SFWM) process, and the Joint Spectral Intensity (JSI) and their relation with the spectral properties of photon sources. In summary, this chapter presents the theoretical framework to be considered in subsequent chapters.

2.2 Maxwell's equations in dielectric media

Macroscopic Maxwell's equations are used to describe the propagation of electromagnetic fields in dielectric and metallic media. The macroscopic Maxwell's equations are given by [26, 27]:

$$\nabla \cdot \tilde{\mathbf{D}}(\mathbf{r}, t) = \rho, \quad (2.1)$$

$$\nabla \cdot \tilde{\mathbf{B}}(\mathbf{r}, t) = 0, \quad (2.2)$$

$$\nabla \times \tilde{\mathbf{E}}(\mathbf{r}, t) = \frac{\partial}{\partial t} \tilde{\mathbf{B}}(\mathbf{r}, t), \quad (2.3)$$

$$\nabla \times \tilde{\mathbf{H}}(\mathbf{r}, t) = \vec{\mathbf{J}} + \frac{\partial}{\partial t} \tilde{\mathbf{D}}(\mathbf{r}, t), \quad (2.4)$$

where ρ is the electric charge density, $\tilde{\mathbf{D}}(\mathbf{r}, t)$ is the displacement field, $\tilde{\mathbf{E}}(\mathbf{r}, t)$ the macroscopic electric field, $\tilde{\mathbf{H}}(\mathbf{r}, t)$ the macroscopic magnetic field, $\tilde{\mathbf{B}}(\mathbf{r}, t)$ the magnetic induction field and $\vec{\mathbf{J}}$ the current density. For a dielectric material, the absence of free charges or currents impose $\rho = 0$ and $\vec{\mathbf{J}} = 0$. The displacement field is related to the electric field, while the induction magnetic field to the magnetic field with the following constitutive equations:

2. THEORETICAL BACKGROUND

$$\tilde{\mathbf{D}}(\mathbf{r}, t) = \varepsilon_0 \varepsilon(\mathbf{r}) \tilde{\mathbf{E}}(\mathbf{r}, t), \quad (2.5)$$

$$\tilde{\mathbf{H}}(\mathbf{r}, t) = \frac{1}{\mu_o \mu(\mathbf{r})} \tilde{\mathbf{B}}(\mathbf{r}, t), \quad (2.6)$$

where ε_0 is the permittivity, and μ_o the permeability of vacuum, ε is the dielectric function of the material, generally this function depends on the position and frequency.

Rewriting the Maxwell's equations and using vectorial identities, we obtain the wave equation for the electric and magnetic fields in dielectric media:

$$\nabla^2 \tilde{\mathbf{E}}(\mathbf{r}, t) - \mu_o \varepsilon_0 n^2 \frac{\partial^2}{\partial t^2} \tilde{\mathbf{E}}(\mathbf{r}, t) + \nabla \left(\frac{\nabla \varepsilon(\mathbf{r})}{\varepsilon(\mathbf{r})} \cdot \tilde{\mathbf{E}}(\mathbf{r}, t) \right) = 0, \quad (2.7)$$

where $\varepsilon = n^2$ [26, 27]. The equation (2.7) is the general wave equation for the electric field. For the magnetic field, we obtain:

$$\nabla^2 \tilde{\mathbf{H}}(\mathbf{r}, t) - \mu_o \varepsilon_0 \frac{\partial^2}{\partial t^2} \tilde{\mathbf{H}}(\mathbf{r}, t) + \frac{1}{\varepsilon(\mathbf{r})} \nabla \varepsilon(\mathbf{r}) \times (\nabla \times \tilde{\mathbf{H}}(\mathbf{r}, t)) = 0. \quad (2.8)$$

Because Maxwell's equations are linear, time and space dependency can be separated by expanding the fields into a set of **harmonic modes**. We can therefore write the fields as a spatial pattern times a complex exponential as:

$$\tilde{\mathbf{E}}(\mathbf{r}, t) = \mathbf{E}(\mathbf{r}) e^{-i\omega t}, \quad (2.9)$$

$$\tilde{\mathbf{H}}(\mathbf{r}, t) = \mathbf{H}(\mathbf{r}) e^{-i\omega t}. \quad (2.10)$$

Equations 2.9 and 2.10 mean that, even if we do not know the spatial distribution of the fields in the media, it is possible to solve the temporal part using separation of variables.

Taking into consideration harmonic modes and using equations (2.4) and (2.3), we obtain the following equation for the magnetic field:

$$\boxed{\nabla \times \left(\frac{1}{\varepsilon(\mathbf{r})} \nabla \times \mathbf{H}(\mathbf{r}) \right) = \left(\frac{\omega}{c} \right)^2 \mathbf{H}(\mathbf{r}).} \quad (2.11)$$

Equation (2.11) is known as the **master equation**, where c is the speed of light, defined as $c = (\mu_o \varepsilon_0)^{-1/2}$ and ω is the angular frequency. A series of operations acts on the magnetic field, and if $\mathbf{H}(\mathbf{r})$ is an allowed mode, the result is a scalar multiplied by the original function $\mathbf{H}(\mathbf{r})$. This treatment can be also applied to the electric field, in this case we have used the magnetic field due to mathematical convenience.

2.2.1 Electromagnetism as an eigenvalue problem

The left-hand side term in the equation (2.11) can be seen as an operator acting on the mode profile $\mathbf{H}(\mathbf{r})$, so we can rewrite it as [28]:

$$\hat{\Theta}\mathbf{H}(\mathbf{r}) = \left(\frac{\omega}{c}\right)^2 \mathbf{H}(\mathbf{r}), \quad (2.12)$$

where the operator $\hat{\Theta}$ is defined by:

$$\hat{\Theta}\mathbf{H}(\mathbf{r}) = \nabla \times \left(\frac{1}{\varepsilon(\mathbf{r})} \nabla \times \mathbf{H}(\mathbf{r}) \right). \quad (2.13)$$

We observe that the action of the operator is: first to take the curl of the vector, then divide by $\varepsilon(\mathbf{r})$ and finally take the curl to the result. The eigenvectors $\mathbf{H}(\mathbf{r})$ are the spatial patterns of the modes and the eigenvalues $(\omega/c)^2$ are proportional to the square of the frequency of those modes. The operator $\hat{\Theta}$ is a linear operator and Hermitian, which implies specific properties that we will present in the following sections.

2.2.1.1 Fundamental properties of eigenmodes

The operator $\hat{\Theta}$ and the vectors fulfill important properties, which are of great utility in the description of the modes. We can observe that the operator $\hat{\Theta}$ is a *linear operator*, that is, if we find the solutions $\mathbf{H}_1(\mathbf{r})$ and $\mathbf{H}_2(\mathbf{r})$ for the master equation, then, a linear combination of both solutions is also a solution for the master equation, that is, $\alpha\mathbf{H}_1(\mathbf{r}) + \beta\mathbf{H}_2(\mathbf{r})$, where, α and β , are constants related to the amplitude probabilities of each mode.

The operator $\hat{\Theta}$ is also a *Hermitian* operator, this is an important characteristic, where $\hat{\Theta}$ satisfies the following properties:

- The eigenvalues of $\hat{\Theta}$ are positive real values, in such a way that, $\omega > 0$.
- $\hat{\Theta} = \hat{\Theta}^\dagger$, that is, the operator is equal to the transposed conjugate.

In addition to hermicity, $\hat{\Theta}$ forces any two harmonic modes with difference frequencies ω_1 and ω_2 to have inner product of zero, that is:

$$(\omega_1^2 - \omega_2^2) \langle \mathbf{H}_1(\mathbf{r}), \mathbf{H}_2(\mathbf{r}) \rangle = 0. \quad (2.14)$$

If $\omega_1 \neq \omega_2$, then $\langle \mathbf{H}_1(\mathbf{r}), \mathbf{H}_2(\mathbf{r}) \rangle = 0$ and the modes are orthogonal. However if $\omega_1 = \omega_2$, then the modes are degenerate and not necessarily orthogonal.

2.2.2 Numerical methods: WMM mode solver and eigenmode expansion

In figure 2.1, the schematic representation of the cross section of a ridge waveguide is shown. The effective refractive index of the waveguide is determined by the width (w),

2. THEORETICAL BACKGROUND

height (h) and the materials. We considered a silicon dioxide substrate on top of a silicon wafer, where the silicon nitride is on top of the SiO_2



Figure 2.1: Cross section of the optical waveguide used for our simulations.

Solving the structure presented in figure 2.1 and obtaining an analytical expression can be difficult but easily solvable by using numerical methods.

There are many different software used for modeling physical systems based on optical and optoelectronic devices, they can be commercial or free use and each one proves advantages or disadvantages. Every software uses a different method in order to solve the system.

In the development of this thesis we used two freely-available software for simulating optical waveguides: *VEIMS Mode Solver and Wave Matching Method (WMM)* in order to obtain the propagation constant (β), the effective refractive index (n_{eff}) and the width of optical waveguides with a height constant for single mode optical waveguides.

2.2.2.1 WMM Mode Solver

VEIMS mode solver and WMM are two different tools used in the design of the optical waveguides, it can be used to find all the eigenmodes allowed in a multilayer system, for a selected mode it shows the effective refractive index and in consequence, the propagation constant. This software also allows one to plot the desired mode. The accuracy of this method relies on the number of spectral terms considered in the calculation which relapse in computing time.

The vectorial effective index method (VEIM) can be viewed as some bridge between two popular approaches, namely the Film Mode Matching (FMM) on the one hand and the effective index method (EIM) on the other [29].

This mode solver is a free software that can be used in any operating system where the main programming language is C++, but it can be implemented only with an interface for easy use. The objective of the use of this mode solver is to find the effective refractive index for different propagating modes in the optical waveguides.

2.2.3 Group refractive index

The group refractive index is an important parameter in the design of resonators. It is defined as the ratio of the vacuum velocity of light to the group velocity in the medium ($n_g = \frac{c}{v_g}$). For optical waveguides it is useful to write it in terms of the effective refractive index as [26, 30, 31]:

$$n_g(\lambda) = n_{eff}(\lambda) - \lambda \frac{d}{d\lambda} n_{eff}(\lambda). \quad (2.15)$$

where λ is the wavelength. As mentioned earlier, the effective refractive index already accounts for both the refractive indices of the materials and the geometry. Therefore, it is convenient to use the effective refractive index for the determination of the group index. In the following sections, we show the importance of these parameters.

2.2.4 Dispersion

It is well known that the refractive index of materials depends on the wavelength, meaning that it is not constant for all wavelengths, a phenomenon known as chromatic dispersion. On the other hand, the combination of different materials and the dimensions play a crucial role when designing optical waveguides [26]. The dispersion can be calculated in terms of the effective refractive index as:

$$D_\lambda = -\frac{\lambda}{c} \frac{d^2}{d\lambda^2} n_{eff}(\lambda). \quad (2.16)$$

Alternatively, the dispersion can be written in terms of the Group Velocity Dispersion (GVD) which is usually referred as: $\beta_2 = \frac{d^2\beta(\omega)}{d\omega^2}$. Then, we have the following relation for the dispersion and the GVD:

$$D_\lambda = -\frac{2\pi c}{\lambda^2} \beta_2. \quad (2.17)$$

In this case, $n_{eff}(\lambda)$ is the effective refractive index of the optical mode, where all the geometrical and optical parameters are already considered.

Furthermore, when $D_\lambda \geq 0$ corresponds to the anomalous dispersion region while $D_\lambda < 0$ corresponds to the normal dispersion region. For nonlinear applications such as supercontinuum or SFWM, it is required that the pump wavelength must be in the anomalous dispersion region, especially in the case of SFWM when the signal and idler photons are expected to be spectrally separated [25]. Hence, it is possible to determine whether the designed optical waveguide is suitable for the specific purpose by calculating and analyzing its dispersion.

2.2.5 Integrated microring resonators

A cavity can be implemented in integrated photonics by using a ring which acts as a resonator. In Fig. 2.2 the schematic representation of a basic ring resonator is shown

2. THEORETICAL BACKGROUND

also called *all-pass ring resonator* [31] which consist of a bus waveguide and a microring. Considering that the light is coupled to the ring resonator, we can consider that there is a small portion of light that goes out every round-trip which can be considered as a mirror with high reflectivity. In this basic scheme, the resonator can be described using the reflectivity r and transmissivity t in such a way that the input field from the bus waveguide is coupled by an evanescent field (transmitted field) and the remaining input field just passes the ring (reflected field).

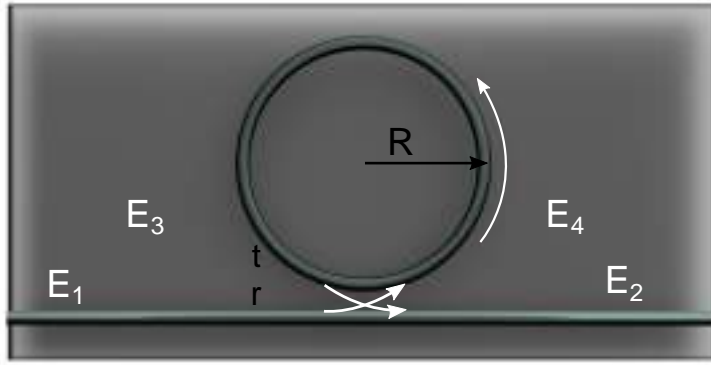


Figure 2.2: Schematic representation of a microring resonator coupled to a bus waveguide.

Considering the input field as E_1 , we can describe the relations between the input and output fields in the matrix form as:

$$\begin{pmatrix} E_1(\omega) \\ E_2(\omega) \end{pmatrix} = \begin{pmatrix} r & it \\ it & r \end{pmatrix} \begin{pmatrix} E_3(\omega) \\ E_4(\omega) \end{pmatrix}. \quad (2.18)$$

Furthermore, considering a lossless cavity, we have that the energy must be conserved, that can be seen through $|r|^2 + |t|^2 = 1$. The field in the resonator acquires a phase shift in terms of the length of the cavity and the propagation constant as $E_3 = Ae^{i\beta L}E_4 = Ae^{i\phi}E_4$, and L corresponding to the cavity length. Then, the transmission of the ring resonator assuming a normalized amplitude ($A = 1$) can be found as:

$$T = \frac{E_3}{E_1} = \frac{it}{1 - re^{i\beta L}}, \quad (2.19)$$

where equation 2.19 has the form of an Airy function that will be used in the following sections. An important aspect is that not all the wavelengths will be resonant in the cavity. This can be obtained by the resonant condition which is written as:

$$\beta L = 2\pi l, \quad (2.20)$$

where l is an integer known as the azimuthal mode number of the whispering gallery modes of the resonator. Hence, the cavity can only propagate wavelengths that satisfy

the resonant condition previously mentioned. Note that to find the resonant angular frequencies, we can rewrite the resonant condition in the following form:

$$\omega_l = \frac{lc}{Rn_{\text{eff}}(\lambda)}. \quad (2.21)$$

By solving equation 2.21, all the resonances can be found. Furthermore, the dependence of the effective refractive index already accounts for chromatic and geometric dispersion.

Since all the resonances become discrete values in the frequency space, it is possible to estimate the difference between two adjacent resonances. However, these differences are not equal due to dispersion. The Free Spectral Range (FSR) is the parameter that quantifies the difference between two resonances and is defined as:

$$FSR(\nu) = \frac{c}{Ln_g(\nu)} = \frac{c}{L(n_{\text{eff}}(\lambda) - \lambda \frac{d}{d\lambda} n_{\text{eff}}(\lambda))}. \quad (2.22)$$

It is important to point out that the FSR can be written as a function of wavelengths or frequencies, and the relationship is different in both cases. In our case, we describe the FSR as a function of frequencies in 2.22 as all the parameters in this work are presented in the frequency domain. Furthermore, note that the FSR depends on the group index. We use the FSR as a parameter for comparison between theoretical and experimental data. This is because the FSR includes the first derivative in its definition, which is sensitive to variations in the refractive index depending on the wavelength. Another important point is that the FSR depends on two parameters: the length of the cavity and the group index, which in turn depends on the geometry and refractive index of the sample. When comparing the theoretical and experimental FSRs, we attribute the small differences to the geometry, which is main source of errors in the fabrication process.

Another important parameter for the design of integrated resonators is the integrated dispersion, which is a function that allows to quantify the deviation of the resonances produced by the dispersion in a resonator [32, 33]. It can be written in terms of the mode index as:

$$D_{\text{int}}(\mu) = \omega_\mu - \omega_0 - \mu D_1, \quad (2.23)$$

where μ is known as the mode index, and $\mu = 0$ represents the pump mode index. Thus, ω_0 corresponds to the pump frequency, and $D_1 = 2\pi FSR(\omega_0)$. Note that for $D_{\text{int}}(\mu = 0) = 0$, meaning that the integrated dispersion is properly centered at the pump frequency. Therefore, the integrated dispersion is not the same for all the frequencies; it strongly depends on the pump frequency. Moreover, we can rewrite the integrated dispersion in terms of the azimuthal mode index. This allow us to work in an easier way since we can determine the discrete frequencies from the resonant condition.

$$D_{int}(\omega) = \omega_l - \omega_0 - (l(\omega) - l_p(\omega_p))D_1. \quad (2.24)$$

where, ω_l , ω_p and l_p are the resonant frequencies, the pump frequency and the pump azimuthal mode. In this scenario, we can clearly manipulate the pump frequency confirming that is not the same tendency for all the frequencies. Note that the equation 2.24 is written as a function of ω but it can be easily replaced by l since these parameters are related [33, 34].

2.3 Nonlinear processes

Considering an electromagnetic field that interacts with a dielectric medium, it can induce a nonlinear response due to the presence of an intense electromagnetic field [30, 35]. This can be described in terms of the polarization P which is related with the strength of the electromagnetic field as:

$$P = \epsilon_0(\chi^{(1)}E + \chi^{(2)}|E|^2 + \chi^{(3)}|E|^3 + \dots), \quad (2.25)$$

where ϵ_0 is the vacuum permittivity, $\chi^{(n)}$ is the nonlinear susceptibility of n -th order. The linear regime of the susceptibilities corresponds to $\chi^{(1)}$, since the polarization is proportional and linear to the electric field. The nonlinear regime includes $\chi^{(2)}$ and $\chi^{(3)}$, where the former represents the second order and the latter the third order.

Nonlinear processes such as Second Harmonic Generation (SHG), Sum Frequency Generation (SFG) or Spontaneous Parametric Down Conversion (SPDC) are related with $\chi^{(2)}$ that occurs in centrosymmetric media, while Third Harmonic Generation (THG) or Spontaneous Four Wave Mixing (SFWM) are nonlinear processes that occur in non-centrosymmetric media related with $\chi^{(3)}$ [35].

2.3.1 Spontaneous Four Wave Mixing

SFWM is a third-order nonlinear process ($\chi^{(3)}$) that involves four frequencies [13]. This process is typically exploited in fibers or integrated waveguides, where two photons from the pump are annihilated to create a pair of correlated photons. Many variants of this process such as co-propagating [7], counter-propagating [36], degenerate pumps or non-degenerate pumps, cross-polarized pumps [37], etc., can be exploited to implement SFWM. The energy conservation when considering degenerate pumps is described by:

$$2\omega_p = \omega_s + \omega_i, \quad (2.26)$$

where ω correspond to the angular frequency and the subscripts p,s and i corresponds to the pump, signal and idler, respectively. In Fig. 2.3 the schematic representation of this process is shown, where the signal photon is denoted with a higher energy that can be written as a function of the pump with a detuning as $\omega_s = \omega_p + \Omega$, while the idler photon is written as $\omega_i = \omega_p - \Omega$ with a lower energy.

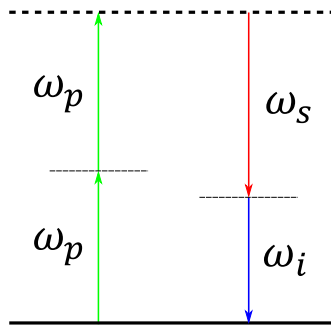


Figure 2.3: Schematic representation of the SFWM, two photons from a pump are annihilated to create a signal and idler photon pair.

In addition to energy conservation, SFWM must satisfy a phase matching condition, according to:

$$\Delta\beta = 2\beta_p(\omega_p) - \beta_s(\omega_s) + \beta_i(\omega_i) - 2\gamma P_0, \quad (2.27)$$

where β is the propagation constant of the optical guided mode, γ is the nonlinear coefficient and P_0 is the pump power [38, 39]. The nonlinear coefficient is one of the most important parameters as it relates to the nonlinear refractive index and the effective area as [39]:

$$\gamma = \frac{n_2\omega_p}{A_{eff}c}, \quad (2.28)$$

with n_2 the nonlinear refractive index of the material. Moreover, A_{eff} is the effective area for the four fields involved which is described as:

$$A_{eff} = \frac{1}{\int \int f_p(x, y)^2 f_s^*(x, y) f_i^*(x, y) dx dy}, \quad (2.29)$$

where the field distributions are normalized as $\int \int |f_j(x, y)|^2 dx dy = 1$, for $j = p, s, i$. Note that the propagation constant is related directly with the effective refractive index. Hence, multiple combinations can be explored such as co-polarized for the TE or TM modes, or cross-polarized. We limited our simulations to the co-polarized case since we want to produce frequency correlated photons with the same polarization as the pump, while the cross-polarized cases will be considered in future work.

2.3.2 Joint Spectral Intensity of SFWM

In this subsection we will describe the theoretical JSI for optical waveguides and integrated resonators, pointing out the differences and advantages of both systems.

One way to characterize the two-photon quantum state generated by a photon source is by analyzing the Joint Spectral Intensity (JSI) function where all the spectral

2. THEORETICAL BACKGROUND

information is contained. The quantum state generated by a SFWM process in an integrated cavity is typically written as [39, 40]:

$$|\Psi_{cav}\rangle = \zeta \sum_{\omega_s} \sum_{\omega_i} G_{cav}(\omega_s, \omega_i) a^\dagger(\omega_s) b^\dagger(\omega_i) |0\rangle_s |0\rangle_i, \quad (2.30)$$

where ζ is a normalization constant, the creation operators are acting over the vacuum state in the signal and idler modes and the function $G_{cav}(\omega_s, \omega_i)$ is known as the Joint Spectral Amplitude (JSA) which contains all the spectral properties of the quantum state and which can be recovered through a measurement of the JSI ($|G_{cav}(\omega_s, \omega_i)|^2$). Hence the JSI in a cavity is typically written as:

$$|G_{cav}(\omega_s, \omega_i)|^2 = |G(\omega_s, \omega_i)|^2 \mathcal{M}_{cav}(\omega_s, \omega_i) \quad (2.31)$$

where $|G(\omega_s, \omega_i)|^2$ is the JSI when the cavity is absent and $\mathcal{M}_{cav}(\omega_s, \omega_i)$ is the matrix of resonances which account for the effect of the cavity over the two-photons state, as defined below. The absent-cavity JSI function is described by the product of the pump envelope function $\alpha(\omega_s, \omega_i)$ and the phase matching function $\phi(\omega_s, \omega_i)$. The pump envelope function describes all the spectral properties of the pump such as the central frequency and bandwidth, while the phase matching function contains all the information of the optical waveguide such as dispersion and propagation length. Hence the JSI is written as:

$$|G(\omega_s, \omega_i)|^2 = \left| \int d\omega' \alpha(\omega') \alpha(\omega_s + \omega_i - \omega') \phi(\omega_s, \omega_i) \right|^2, \quad (2.32)$$

with the pump envelope described by a Gaussian function as:

$$\alpha(\omega_s, \omega_i) = e^{-\frac{(\omega_s + \omega_i - 2\omega_p)^2}{2\sigma^2}}, \quad (2.33)$$

where $\sigma = \frac{2\pi\delta\nu_p}{\sqrt{2\log(2)}}$ and $\delta\nu_p$ corresponds to the linewidth of the pump, while the phase matching function is written as:

$$\phi(\omega_s, \omega_i) = \text{sinc}\left(\frac{L}{2}\Delta\beta(\omega_s, \omega_i)\right) e^{i\frac{L}{2}\Delta\beta(\omega_s, \omega_i)}. \quad (2.34)$$

All the spectral properties of the material and geometry of the waveguide are contained in the phase matching function. In this way, the JSI relates the pump parameters with the geometrical and optical parameters of the material through these two functions.

The matrix that describes the cavity effect is written as the product of two Airy functions, one is acting over ω_s and the other acting over ω_i . In this way, we can represent the matrix of resonances as:

$$\mathcal{M}_{cav}(\omega_s, \omega_i) = \mathcal{A}_s(\omega_s) \mathcal{A}_i(\omega_i), \quad (2.35)$$

where the Airy function $A_\mu(\omega_\mu)$ describes the effect of the resonator over the photon pair state, with the internal resonance enhancement factor given by [39, 41]:

$$A_\mu(\omega_\mu) = \frac{t_\mu(\omega_\mu)}{1 - r_\mu(\omega_\mu) \exp[i\beta_\mu(\omega_\mu)L]}, \quad (2.36)$$

where t_μ and $|r_\mu(\omega_\mu)| = 1 - l(\omega_\mu)\pi Q^{-1}$ are the transmissivity and reflectivity amplitudes of the ring and the argument of the exponential represents the phase acquired by the photon $\mu = s, i$ in one round-trip. Then, the resonances appear at the peaks of the Airy function which we previously defined as the resonance condition. Note that we have included the dependence with t and r coefficients which in an experimental implementation is important. In the following chapter we will show the overall behavior of these functions.

2.4 Conclusion

In the present chapter, we provided the theoretical background for optical waveguides and quantum optics. Additionally, we described the microring resonators and the most important parameters that must be taken into account for our design of a photon source such as: dispersion, integrated dispersion and FSR. In addition, we detailed the SFWM non-linear process that can be generated in optical waveguides. Furthermore, the theoretical description for the JSI is detailed, which is useful to describe a two-photon quantum state and its spectral properties. In conclusion, this chapter provides the equations and a short description of them, which are used in the following two chapters.

Integrated photon pairs source compatible with a quantum memory

3.1 Introduction

Optical quantum communications is a promising emergent technology which requires the development of several new quantum devices to carry and store quantum information over long distances [42, 43, 44, 45]. One of such devices is the quantum repeater which, as their classical counterparts, is needed to maintain the properties of entangled photonic states over propagation through the future quantum networks. Nowadays, quantum repeaters are based on quantum memories that store and release on demand single photons in media such as atoms, molecules, or ions [42, 44, 45]. One of the main challenges for quantum memories is an efficient interaction between photons and the media used to store information such as a match between the spectral properties of the input photons and the resonances of the atomic species in the media [43, 44, 46].

In particular, Y_2SiO_5 crystal doped with Pr^{3+} ions has been demonstrated as a suitable candidate for quantum memories due to its interesting properties such as long decoherence time and easy compatibility with fiber networks. [44, 47]. Typically, these atomic species are excited using photons generated by the spontaneous parametric down conversion process (SPDC) using bulk crystals, for example, BBO, PPLN, PP-KTP among some others. In this case, the spectral bandwidth of the photons has been achieved by using free space cavities [45, 48], which present an intrinsic limitation in the sense that bulky setups turn free-space cavities impractical when thinking in scalable applications.

The platform of silicon nitride (Si_3N_4) is considered as an optimal platform for the design of the photon source since this material has a larger refractive index, but not too high in comparison with SOI, AlGaAs or 4H-SiC. This allows the phase matching at short wavelengths, and moreover, this material has been recently shown as a suitable platform for enabling devices in visible wavelengths [49, 50, 51, 52].

In this chapter, we describe the procedure for designing an integrated photon

pair source based on a microring resonator that matches the spectral properties of praseodymium ions in a crystal ($\text{Pr}^{3+}:\text{Y}_2\text{SiO}_5$). In this setup, the signal and idler photons are on-chip and separated by the add-drop configuration. Moreover, the signal photon can be sent directly to the solid-state quantum memory, while the idler photon can be directed to a CWDM for simultaneous detection after the interaction of the signal photon with the quantum memory.

First, the wavelengths of the photons are determined by the phase-matching condition, which is engineered by adjusting the width of the waveguides. This change alters the effective refractive index and the dispersion profile. Additionally, the spectral properties of the two-photon quantum state are analyzed through the Joint Spectral Intensity (JSI), which provides the wavelength and bandwidth of the photons.

3.2 Design of the integrated photon source

Silicon nitride is a material that in addition to its interesting nonlinear refractive index n_2 , possesses a high refractive index providing a high refractive index contrast for air and SiO_2 claddings. Along with that, it can provide high compatibility to generate photons in visible-telecom wavelengths due to its transparency window. Consequently, our proposed photon source takes advantage of these interesting properties.

On the other hand, the spectral properties of the photon source are tailored to match the spectral properties of the $\text{Pr}^{3+}:\text{Y}_2\text{SiO}_5$ crystal. This can be accomplished by properly choosing the cross section of the waveguide such that the SFWM can be achieved providing the proper wavelength and by using an integrated cavity that can reduce the bandwidth of the photons and simultaneously enhance the photon pair generation.

In Figure 3.1 a) the schematic representation of the proposed device is shown. It consists of a ring resonator using an add-drop configuration while in figure 3.1 b) the energy levels of the Pr^{3+} ion are shown, where the specific wavelength between the levels ${}^3H_4 \leftrightarrow {}^1D_2$ at 606 nm and the bandwidth between the transitions is around 4 MHz.

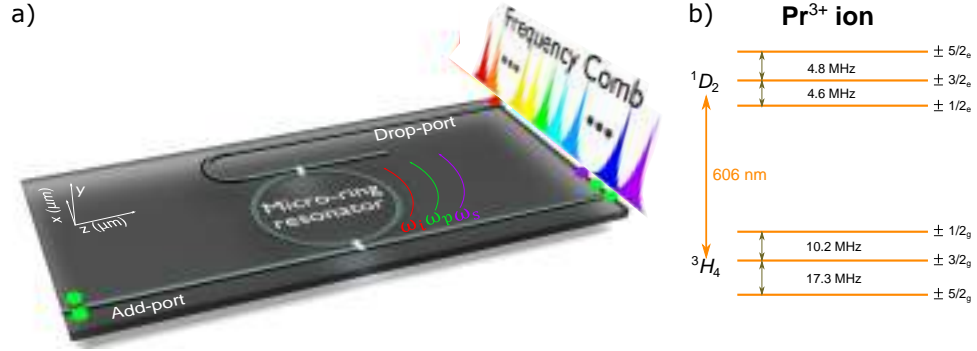


Figure 3.1: a) Schematic representation of an integrated photon source based on SFWM using a microring resonator that produces photon pairs capable of interacting with a $\text{Pr}^{3+}:\text{Y}_2\text{SiO}_5$ solid state quantum memory, and b) scheme of energy levels of $\text{Pr}^{3+}:\text{Y}_2\text{SiO}_5$ crystal.

A few considerations must be taken into account for the design of the photon source involving the wavelength of the praseodymium ions, the pump wavelength source and detection which are described as follows:

- The wavelength of the signal photon is fixed at $\lambda_s = 606$ nm that matches the atomic transition $^3H_4 \leftrightarrow ^1D_2$ of the praseodymium ions.
- The pump wavelength must be a commercially available continuous wave laser with a narrow linewidth.
- The idler wavelength must match a CWDM channel [53], and be within the window of detection of current InGaAs or Superconducting Nanowire single-Photon Detector (SNSPDs) detectors.

With the previous restrictions, the pump wavelength is determined by using the energy conservation equation written in terms of signal and idler wavelengths as:

$$\lambda_p = \frac{2\lambda_s\lambda_i}{\lambda_s + \lambda_i}, \quad (3.1)$$

where the idler frequency is chosen at $\lambda_i = 1430.5$ nm to match the ITU channel 43 of a CWDM system. In table 3.1 the wavelengths for the pump, signal and idler are shown.

Pump λ_p (nm)	Signal λ_s (nm)	Idler λ_i (nm)
851.347	606	1430.5

Table 3.1: Wavelengths of the pump, signal and idler, where the pump wavelength is determined by using equation 3.1.

3. PHOTON SOURCE FOR A QUANTUM MEMORY

Thus, the pump wavelength matches the specifications of a commercially available laser system (Newport TLB6817) with bandwidth $\delta\nu_p = 200$ kHz [54].

Then, it is necessary to obtain the geometrical parameters of the device that can achieve efficiently the phase matching at the desired wavelengths. To do that, the first step is simulate the waveguide.

The effective refractive index is obtained using WMM solver software by simulating the Si_3N_4 on insulator ridge waveguide shown in figure 3.2. It consist of a silicon wafer with a 2 μm thick SiO_2 layer and, on top of it the Si_3N_4 layer.

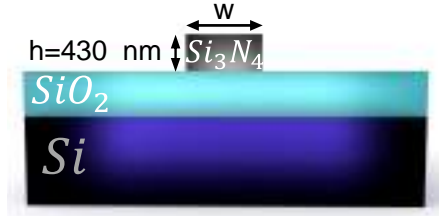


Figure 3.2: Cross section of a Si_3N_4 on insulator ridge waveguide with air cladding.

In order to increase the confinement of the optical mode in the waveguide and simultaneously reduce the complexity in the fabrication process, accessible at our facilities, air has been considered as a surrounding medium. In this case, the only degree of freedom is the width (w) of the waveguide since the height (h) can not be modified with our current electron-beam fabrication process, leaving the width as the only geometrical control parameter [24].

3.3 Effective refractive index and dispersion

For the simulations, the refractive index of the bulk Si_3N_4 and SiO_2 , described by the following two Sellmeier equations [55, 56], is considered:

$$n_{\text{Si}_3\text{N}_4} = \sqrt{1 + \frac{3.0249\lambda^2}{\lambda^2 - 0.1353406^2} + \frac{40314\lambda^2}{\lambda^2 - 1239.842^2}}, \quad (3.2)$$

$$n_{\text{SiO}_2} = \sqrt{1 + \frac{0.6961663\lambda^2}{\lambda^2 - 0.0684043^2} + \frac{0.4079426\lambda^2}{\lambda^2 - 0.1162414^2} + \frac{0.8974794\lambda^2}{\lambda^2 - 9.896161^2}}. \quad (3.3)$$

Figure 3.3 shows the effective refractive index as a function of the wavelength for the TE_{00} (solid line) and TM_{00} (dashed line) modes, for different waveguide widths

and considering a fixed height $h = 430$ nm, as well as the bulk Si_3N_4 and SiO_2 . In this case, the guided mode must satisfy that the effective refractive index is higher than the substrate, this means that, $n_{\text{Si}_3\text{N}_4} > n_{\text{eff}} > n_{\text{SiO}_2}$ for the three wavelengths of interest. We started our analysis by simulating waveguides with width of 400 nm to 1000 nm with steps of 100 nm and analyzing the phase-matching condition. Once we obtained that the optimal geometry was in the range between 700 nm and 900 nm, we simulated geometries with steps of 50 nm. We delimited the region by decreasing the region of interest until finding the optimal geometry. To make a comparison, the effective refractive index of widths 750, 800, 818 and 850 nm is shown.

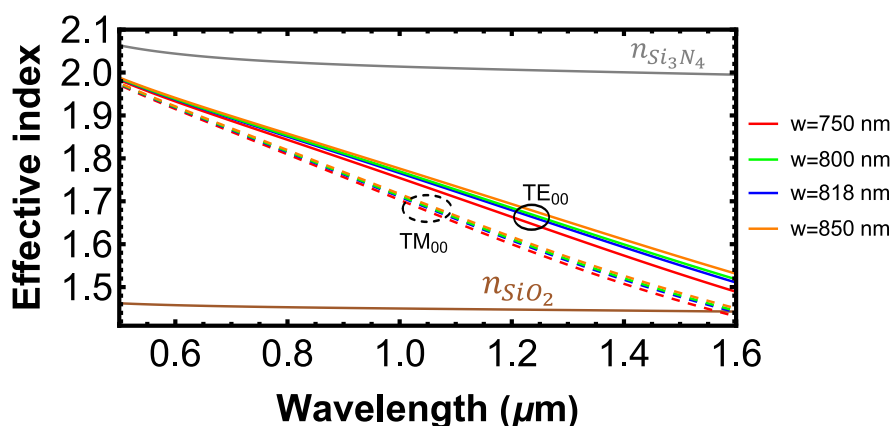


Figure 3.3: Effective refractive index as a function of the wavelength for different widths and a fixed height of $h = 430$ nm for the TE_{00} (solid line) and TM_{00} (dashed line) modes. $n_{\text{Si}_3\text{N}_4}$ and SiO_2 bulk refractive indices are used to delimit the guided modes ($n_{\text{eff}} > n_{\text{SiO}_2}$).

It can be seen that the effective refractive index of the TE_{00} is higher than the effective refractive index of the TM_{00} , thus, the dominant mode for these waveguides is the TE_{00} mode.

As previously mentioned, our photon source is engineered to target specific wavelengths of interest, which is, the case where the photons are wide spectrally separated from the pump. To find the optimal width, we calculate the dispersion parameter where for the pump wavelength which must be within the anomalous dispersion region.

In figure 3.4 the dispersion parameter D_λ is shown for the four different widths as a function of the wavelength. Here, the dispersion already contains the chromatic dispersion and the effect of the dispersion due to the geometrical configuration. The gray zone shows the anomalous dispersion region ($D_\lambda > 0$) for the waveguide with width of 818 nm. It can be clearly seen that when the width is increased, the dispersion is slightly shifted to larger wavelengths as well as reducing the maximum value of dispersion. Furthermore, two Zero Dispersion Wavelength's (ZDW) are found at $\text{ZDW}_1 = 815$ nm and $\text{ZDW}_2 = 1200$ nm for the same geometry. Note that the ZDWs are not the same for all the geometries.

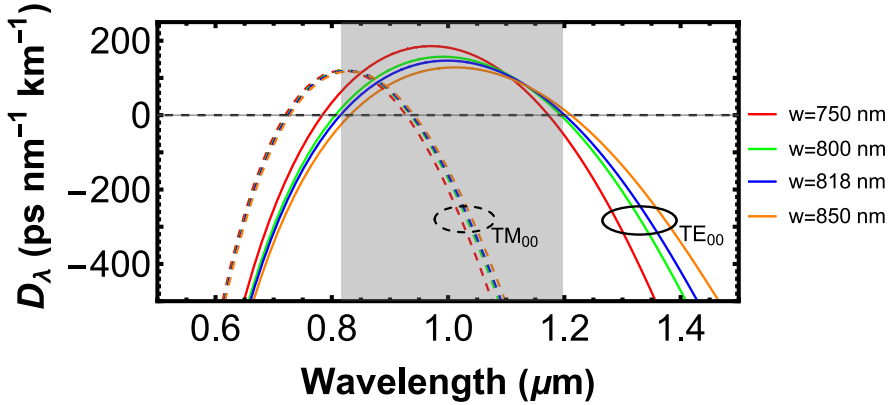


Figure 3.4: Dispersion parameter for TE_{00} and TM_{00} modes. The gray zone delimits the anomalous dispersion $D_\lambda > 0$ for a waveguide with $w = 818 \text{ nm}$ and $h = 430 \text{ nm}$ considering the TE_{00} mode.

Another important fact is that the dispersion for the TM_{00} modes provides anomalous dispersion at the pump wavelength. Although, it does not provide direct information about the phase matching and in consequence, the wavelength of the photons. Therefore, the first step in the design process is to find the widths with anomalous dispersion in the pump wavelength and then, analyze it by plotting the phase matching condition.

3.4 SFWM phase-matching condition

The phase matching condition that provides the satisfying SFWM frequencies is plotted in terms of the frequency detuning, $\Omega_{i,s} = \pm(\omega_p - \omega_{i,s})$, in the following figures for the TE_{00} and TM_{00} . Only the upper half contour is plotted since the lower half is symmetric at $\Omega = 0$. In order to find the optimal geometry that allows emission at the desired wavelengths, two lines are plotted: $\Omega_s = -\omega_p + 2\pi c/0.606$ and $\Omega_i = \omega_p - 2\pi c/1.4305$ in the $(\Omega_{s,i}, \omega_p)$ -space, where the negative and positive slopes are for signal and idler photons, respectively. The intersection of the two lines corresponds to the pump frequency satisfying energy conservation and giving the value of the pump frequency.

3.4.1 Phase-matching for the TM mode

First we will analyze the phase matching condition through the contour plots for the TM_{00} mode.

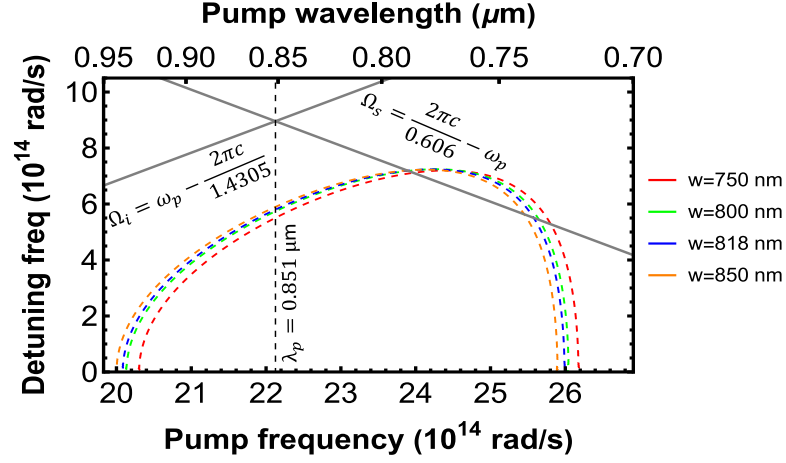


Figure 3.5: Contour plots of the phase-matching condition in terms of the detuning frequency $\Omega_{s,i}$ for the TM_{00} mode i.e., $\Delta\beta(\omega) = 0$.

In figure 3.5, the contour plots of the phase matching for the TM_{00} mode are shown. Here the vertical line shows the pump wavelength $\lambda_p = 851.347$ nm. It can be observed that none of these contour plots of the TM_{00} mode intersects with the two gray lines making unfeasible the use of these modes for our purpose. However, the line Ω_s corresponding to the photons at 606 nm, crosses with the contour plots at different pump frequencies, where the idler photons will have wavelengths that are not available at our detection system.

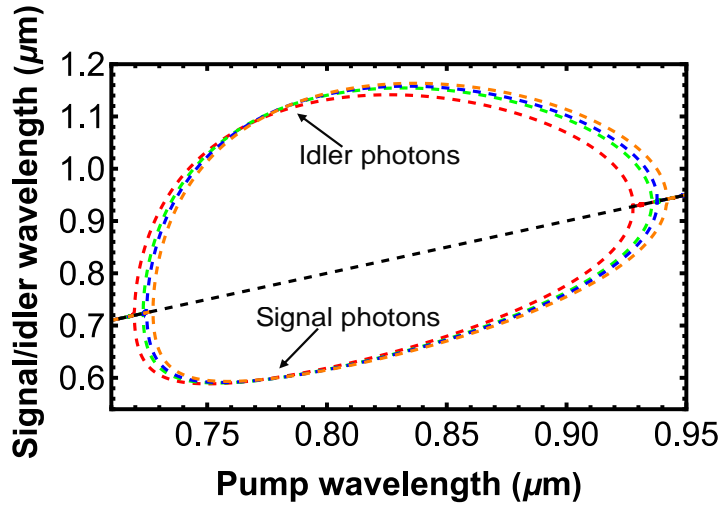


Figure 3.6: Wavelength of the signal and idler photons as a function of the pump wavelength for the TM_{00} mode.

In figure 3.6, the signal and idler wavelengths as a function of the pump wavelengths

3. PHOTON SOURCE FOR A QUANTUM MEMORY

are plotted. There are some possibilities that generate photons at 606 nm, by properly choosing the pump wavelength, but the idler photon will be expected at wavelengths between 1 μm and 1.2 μm where our detector has low quantum efficiency of detection [57]. As an example, the geometry with $w = 818$ nm is expected to generate a photon pair $\lambda_s = 606\text{nm}$ and $\lambda_i = 1127.88$ nm, with a pump wavelength $\lambda_p = 788.4$ nm.

3.4.2 Phase-matching for the TE mode

On the other hand, this difficulty is overcome when the TE mode is chosen. In figure 3.7 the contour plot of the phase matching condition is shown. Note that in this case, we focus on finding the contour that intersects with the two gray lines used to delimit the signal and idler frequencies.

Firstly, we determined the effective refractive index in the range between 750 and 850 nm with steps of 50 nm increase in the width. We observed that the optimal width is between 800 and 850 nm, we estimated the effective refractive index by sweeping the width with steps of 2 nm.

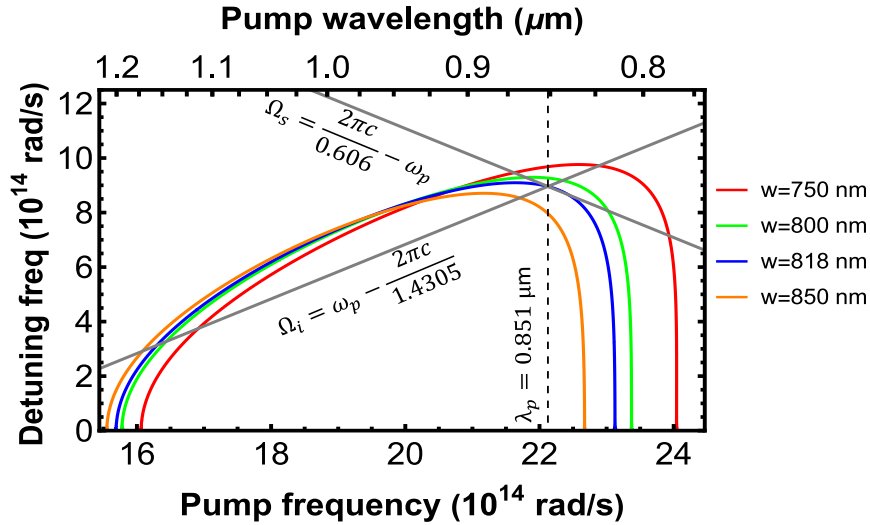


Figure 3.7: Contour plots of the phase-matching condition in terms of the detuning frequency $\Omega_{s,i}$ for the TE_{00} mode i.e., $\Delta\beta(\omega_p) = 0$.

We find that the optimal width is 818 nm making then the cross section of the waveguide to $w = 818$ nm and $h = 430$ nm. In figure 3.8 the signal and idler wavelengths as a function of the pump wavelength for the TE_{00} mode are shown. In a similar way, it can be observed that there are other cases for the generation of photons at 606 nm, while the idler photon will be now expected at larger wavelengths.

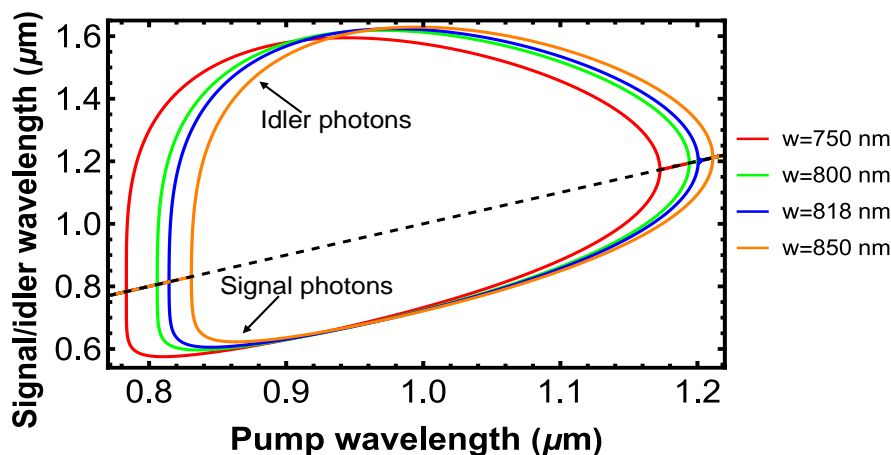


Figure 3.8: Wavelength of the signal and idler photons as a function of the pump wavelength for the TE_{00} mode.

3.5 Integrated dispersion and frequency mismatch

After finding the optimal cross section that allows the phase matching at $\lambda_s = 606$ nm, the second step is to obtain the radius of the resonator in order to obtain all the geometrical parameters of the resonator. Due to the dispersion of the waveguide, the resonances are not perfectly equidistant in the frequency, this effect can not be avoided but it is possible to compensate by properly selecting the radius.

In the context of microring resonators, the integrated dispersion (D_{int}) can be used to quantify and optimize the deviation of the resonance frequency from the equidistant grid given by the free spectral range (FSR) of the resonator [32].

For the proposed integrated cavity we performed simulations to find the optimal radius. There are multiple radii that can be resonant at the desired wavelengths, but just a few could be considered for our calculations since the resonances can be slightly shifted from the desired wavelengths, this means that, these radii could not be optimal even if they could support the pump, signal, and idler photons simultaneously. As a result, when finding the optimal radius, the resonances will be located at the desired wavelengths and in consequence, the JSI (in the cavity absence) maximizes the overlapping with the cavity functions to obtain the final quantum state of the photons produced in the cavity.

To find the optimal radius, first we obtain those radii that satisfy the resonance condition ($\beta L = 2\pi l$) for the three desired wavelengths. Then we estimated the integrated dispersion for the signal and idler photons where the signal and idler wavelengths must have the same value of the integrated dispersion but opposite sign as the sum over them is approximately equal to zero. This can be written as:

3. PHOTON SOURCE FOR A QUANTUM MEMORY

$$D_{int}(\nu_s)/2\pi + D_{int}(\nu_i)/2\pi \approx 0 \quad (3.4)$$

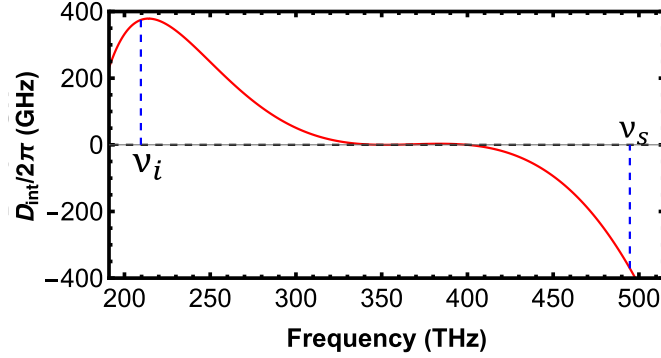


Figure 3.9: Integrated dispersion as a function of the frequency when the pump frequency is centered at $\nu_p = 352.139$ THz.

Figure 3.9 shows the integrated dispersion as a function of the frequency for the radius $R = 155.255 \mu\text{m}$ giving the value of the signal photon (ν_s) with a negative value ($D_{int}(\nu_s)/2\pi = -374.0681$ GHz) and the idler photon (ν_i) with a positive value ($D_{int}(\nu_i)/2\pi = 374.0682$ GHz), which satisfies the previous equation as $D_{int}(\nu_s)/2\pi + D_{int}(\nu_i)/2\pi \approx 0$.

To show the tendency of the radius, we select two different radii that are close to the optimal frequency but that do not satisfy completely the conservation energy and has a slight deviation. This optimization is very important since it is required that the final quantum state is not shifted more than the bandwidth of the Pr ions, that is 4 MHz. In table 3.2 the radii with their respective resonances for the pump, signal and idler photons are shown. It can be seen that the differences are in the order of pm, but this affects directly in the JSI.

Radius (μm)	Pump λ_p (nm)	Signal λ_s (nm)	Idler λ_i (nm)
152.814	851.344	605.9997	1430.482
155.255	851.347	606	1430.5
159.989	851.343	605.9999	1430.483

Table 3.2: Radius and wavelength of the resonances for the pump, signal and idler, where the resonances are determined by the resonance condition ($\beta L = 2\pi l$).

When calculating the resonance condition in the cavity functions, the dispersion of the waveguide is already considered. Hence, the linewidth of the resonances is clearly visible in the cavity functions since they appear in the reflectivity and transmissivity functions as:

$$A_\mu(\omega_\mu) = \frac{t_\mu(\omega_\mu)}{1 - r_\mu(\omega_\mu) e^{i\beta_\mu(\omega_\mu)L}} \quad (3.5)$$

The expected linewidths of the resonances are $\delta\nu_s=14.33$ MHz and $\delta\nu_i=6.07$ MHz. Despite this, the bandwidth of the photons is analyzed through the JSI. We want to point out that the bandwidth of the photons is reduced as well because of the linewidth of the laser that we chose.

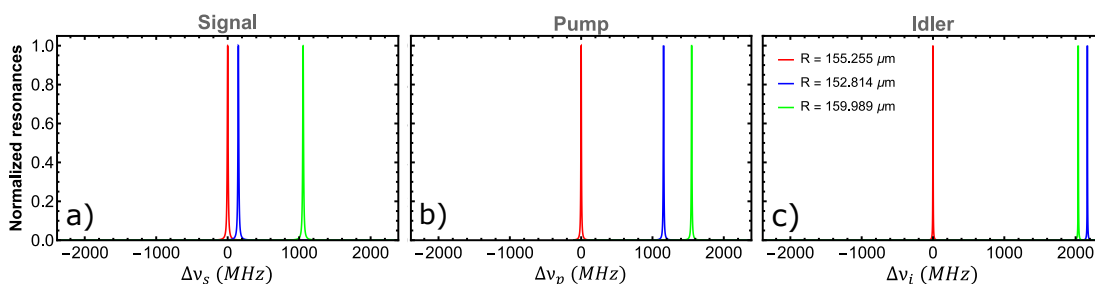


Figure 3.10: Normalized resonances for the three different radii and for the pump, signal and idler photons, respectively, centered at the optimal frequencies.

In figure 3.10 the expected resonances for the three different radii are shown, for the signal, pump and idler respectively. The plots are centered at the frequencies where the perfect phase matching occurs. The play role of the dispersion can be seen because the resonances are slightly shifted. The resonances are normalized and it is clear that for the optimal radius, the shift is minimum. On the other hand, for the nonoptimal radii, it can be observed that in some cases the shifting is higher than 1 GHz, but this does not provide information about the two photon quantum state.

To quantify the overall effect of the shifting we calculated the frequency mismatch which is calculated in terms of the frequencies of the resonances shown in table 3.2 as follows:

$$\Delta\nu = 2\nu_p - \nu_s - \nu_i \quad (3.6)$$

In figure 3.11 the frequency mismatch for the three radii considered is shown. The frequency mismatch affects directly the cavity JSI and in consequence the number of photon pairs generated for the device. Therefore, we focus on minimizing the frequency mismatch in such a way that the number of photons is maximized. For the radius $R = 155.255 \mu\text{m}$ we obtain a frequency mismatch $\Delta\nu \approx 0$ which has been optimize through the integrated dispersion.

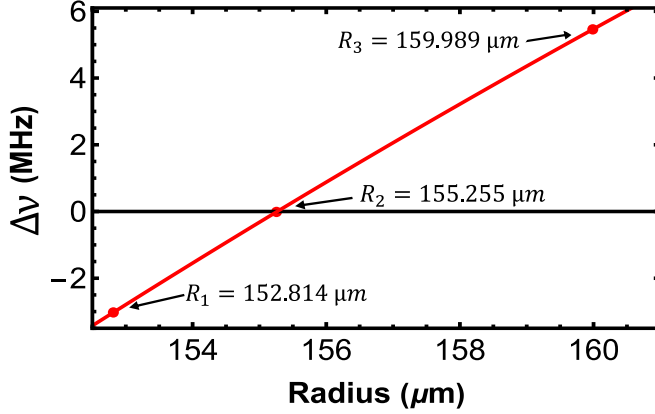


Figure 3.11: Frequency mismatch for three different ring radii where the minimal frequency mismatch is obtained at the optimal ring radius.

3.6 Two-photon quantum state of the cavity

The last step in our design process is the determination of the Q-factor that provides the $\Delta\nu_s = 4$ MHz required bandwidth of the photons which is limited to match the linewidth of the atomic transition of the Pr ions. The determination of the Q-factor is carried out through the analysis of the cavity JSI.

There are two critical parameters in the design which affects the required bandwidth for the signal photon. The first parameter is the Q-factor, mainly determined by the quality of the fabrication process and the second parameter is the bandwidth of the pump laser.

The spectral properties of the SFMW two-photon state are plotted in the figures 3.12, 3.13 and 3.14 in the ν_s, ν_i space, for the obtained Si_3N_4 microring resonator ($w = 818$ nm, $h = 430$ nm) and for the three different radii. The optimal configuration is framed and corresponds to $R_2 = 155.255$ μm .

For the three figures, a) shows the JSI ($|G(\nu_s, \nu_i)|^2$) in the cavity absence scenario obtained from equation 2.32, which corresponds to the product between the pump envelope function and the phase matching function when considering a CW laser with a linewidth $\delta\nu_p = 200$ kHz. In b) the cavity effect due to the microring resonator represented by the matrix 2.35 is shown. As an important observation, the function is not symmetric due to the consideration of the frequency dependence of the reflectivity and transmissivity functions. Finally, c) shows the final two-photon quantum state ($F_{cav}(\nu_s, \nu_i)$) obtained with the equation 2.31, which corresponds to the product between the function $|G(\nu_s, \nu_i)|^2$ in the cavity absence scenario and the matrix $\mathcal{M}_{cav}(\nu_s, \nu_i)$.

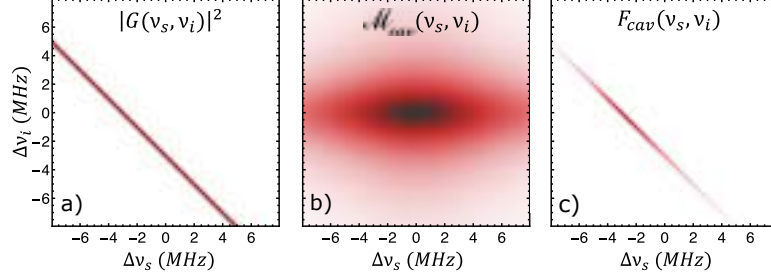


Figure 3.12: Simulation of the JSI for the two-photon quantum state generated by the proposed microring resonator in the (ν_s, ν_i) space for one nonoptimal radius ($R_1 = 152.814 \mu\text{m}$). a) JSI calculated in the cavity absence, b) cavity effect obtained by the resonator and c) resulting cavity-enhanced JSI.

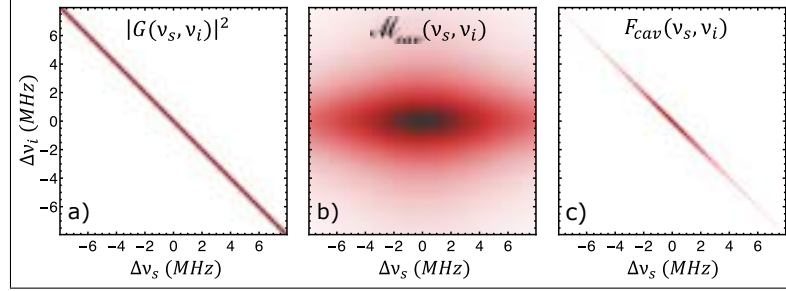


Figure 3.13: Simulation of the JSI for the two-photon quantum state generated by the proposed microring resonator in the (ν_s, ν_i) space for the optimal radius ($R_2 = 155.255 \mu\text{m}$). a) JSI calculated in the cavity absence, b) cavity effect obtained by the resonator and c) resulting cavity-enhanced JSI.

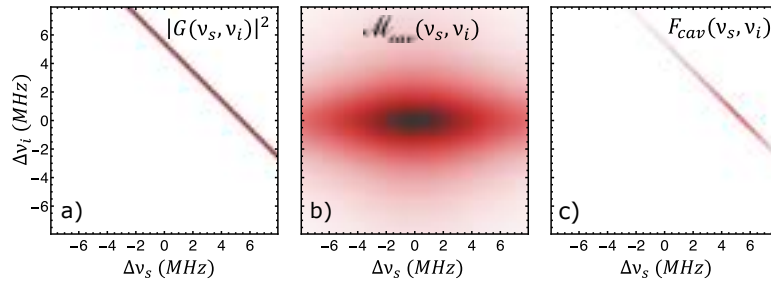


Figure 3.14: Simulation of the JSI for the two-photon quantum state generated by the proposed microring resonator in the (ν_s, ν_i) space for one nonoptimal radius ($R_3 = 159.989 \mu\text{m}$). a) JSI calculated in the cavity absence, b) cavity effect obtained by the resonator and c) resulting cavity-enhanced JSI.

Note that all the plots (figure 3.12, 3.13 and 3.14) are centered at the resonant frequencies ν_s and ν_i for their corresponding radius. For R_1 and R_3 the deviation discussed in the integrated dispersion section is clear, where the $|G(\nu_s, \nu_i)|^2$ function

does not overlap with the cavity function $\mathcal{M}_{cav}(\nu_s, \nu_i)$ in the center, this results in the final quantum state having a lower amplitude compared to the optimal radius. From these deviations, we observe that the signal and idler photons will not be optimally produced at the desired wavelengths, with deviations of a few MHz. Furthermore, these deviations in the non-optimal JSIs directly affect the photon flux, producing fewer photons compared to the optimal configuration.

3.7 Bandwidth determination of the photon source

Finally to obtain the minimal Q-factor needed to attain the bandwidth of the signal photon, the function $F_{cav}(\nu_s, \nu_i)$ is integrated over the idler frequency and normalized (usually referred as the marginal JSI function). The bandwidth of the photons is estimated at FWHM of the marginal JSI function.

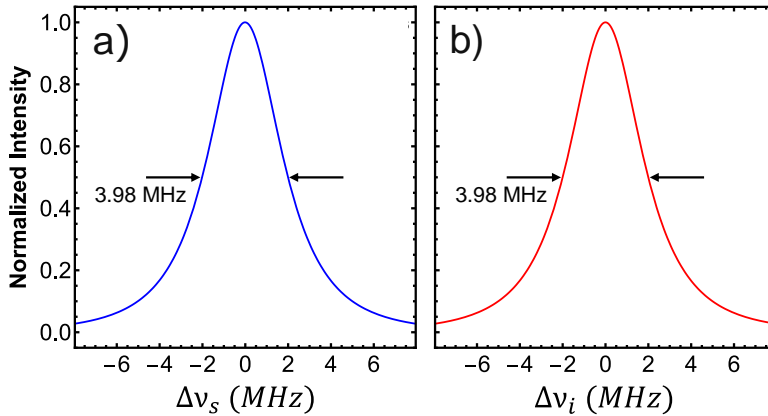


Figure 3.15: Normalized marginal functions obtained by integrating the JSI a) over the idler frequency ν_i and b) over the signal frequency ν_s . The spectral bandwidth is obtained at the FWHM giving a value of $\Delta\nu_{s,i} = 3.98$ MHz for both photons.

In figure 3.15 a) the normalized marginal function is shown, which is integrated over the idler frequency, and that allows to determine the bandwidth of the signal photon, while in b) is shown the normalized marginal function which is integrated over the signal frequency and that allows to determine the bandwidth of the idler photon.

For our device, we determined a minimal Q-factor of $Q_s = 34.5 \times 10^6$ required to achieve a signal photon bandwidth of $\Delta\nu_s = 3.98$ MHz. The bandwidth of the idler photon is estimated with the same procedure obtaining $\Delta\nu_i = 3.98$ MHz.

On the other hand, in the schematic of our proposed integrated photon source (see figure 3.1 a)), we utilize a standard add-drop configuration to separate the signal and idler photons. The add waveguide is specifically designed to couple only the pump and signal photons, set at a width of $w = 550$ nm, with cut-off wavelength at 1390 nm,

while the drop port has the same width of the resonator $w = 818$ nm. As a result, the idler photon is outcoupled through the drop port, making it compatible with a standard telecommunications CWDM system at ITU Channel 43, which is centered at a wavelength of 1430 nm.

After establishing the widths for the add and drop ports, we determined the gap required for each of them with the ring resonator. The add port is designed to have a gap of 190 nm, while the drop port is estimated to have a gap of 460 nm. Both dimensions can be easily achieved using the lithography process available in our facilities, ensuring the necessary Q-factor for our proposed photon source.

3.8 Photon pair generation estimation

After determining all the geometrical parameters for our proposed photon source, we determined the photon flux of our cavity. This can be estimated using the equation when considering a CW laser as:

$$N_{cw} = \frac{2^5 c^2 n_{eff}^2(\omega_p) L^2 \gamma^2 P_0^2}{\pi \omega_p^2} \int d\omega \frac{\omega(2\omega_p - \omega) \beta'(\omega) \beta'(2\omega_p - \omega)}{n_{eff}^2(\omega) n_{eff}^2(2\omega_p - \omega)} \times \mathcal{M}_{cav}(\omega, 2\omega_p - \omega) \text{sinc}^2\left(\frac{L\Delta\beta_{cw}}{2}\right), \quad (3.7)$$

where $\gamma = \frac{n_2 \omega_p}{c A_{eff}}$. To calculate the effective area is needed to obtain the norm of the electric field distribution for the signal, pump and idler photons.

In figure 3.16 the norm of the electric field distributions for the signal, pump and idler photons at their respective wavelengths are shown.

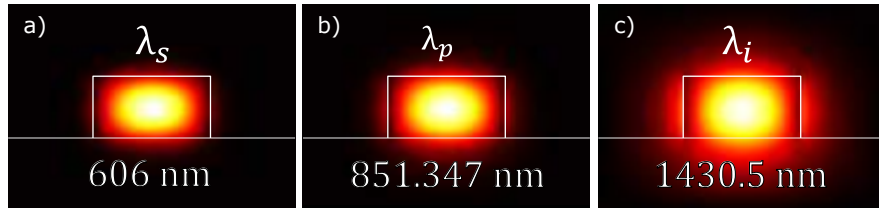


Figure 3.16: Norm of the electric field distribution of the TE₀₀ mode for the a) signal ($\lambda_s = 606$ nm), b) pump ($\lambda_p = 851.347$ nm) and c) idler ($\lambda_i = 1430.5$ nm) photons.

Using equation 2.29, the effective area is estimated, which gives $A_{eff} = 0.328 \mu m^2$. Then the flux of photon pairs expected for our photon source is $N_{cw} = 3.11 \times 10^6$ pairs/s with $P_0 = 1$ mW and a cavity enhancement $E = 1.24 \times 10^4$ which describes the flux enhancement mainly due to the use of the cavity configuration.

3.9 Conclusion

In the present chapter, we outlined the detailed process for the design of an integrated photon source specifically tailored to match the spectral properties of a solid state quantum memory based on a $\text{Pr}^{3+}:\text{Y}_2\text{SiO}_5$ crystal. Our photon source achieves photons spectrally wide separated from the pump by using an enhanced cavity design, while also taking into account the use of a continuous-wave laser and the detection system available at our facilities.

The design process begins with the calculation of the effective refractive index for several widths. Following this, we analyze the dispersion parameter, and then the phase matching condition is analyzed for the TE_{00} and TM_{00} modes.

After this, we carried out simulations to optimize the radius of our photon source through the integrated dispersion and then, we calculated the frequency mismatch for different radii.

Finally, we determined the two-photon quantum state as well as the minimal Q-factor required for our photon source to achieve the bandwidth of the atomic transition of the Pr ions. Additionally, we estimated the flux of photons expected for our integrated cavity.

In summary, these are the all the parameters obtained for our photon source. The optimal geometric parameters for the Si_3N_4 resonator are: $w = 818$ nm, $h = 430$ nm with a radius of $R = 155.255$ μm . The phase matching is achieved to produce signal photons at $\lambda_s = 606$ nm with a spectral bandwidth of $\Delta\nu_s = 3.98$ MHz and idler photons at $\lambda_i = 1430.5$ nm with a spectral bandwidth $\Delta\nu_i = 3.99$ MHz when a CW laser is considered at $\lambda_p = 851.347$ nm with $\delta\nu_p = 200$ kHz linewidth. Furthermore, the minimal Q-factor required to match the signal photon and the Pr ions bandwidth is $Q_s = 34.5 \times 10^6$. It needs to be pointed out that this Q-factor has not been already reached out due to limitations in the fabrication process which affect the quality of the device, but once it can be overcome, is suitable for its implementation.

Note: The steps followed in the simulations constitute a recursive process, meaning that slight variations in the geometry directly impact the phase-matching condition and the resulting two-photon quantum state. The graphs presented in this chapter are considered the optimal parameters found in the design process.

Broadband Frequency Comb Generation by Dispersion Engineering

4.1 Introduction

Integrated photonic quantum technologies is a field of research that has been growing in the last decades with potential applications in sensing [58], quantum metrology [59] and quantum communications [60] among others [61, 62, 63, 64]. In particular, integrated photon sources based on SPDC or SFWM process [15], have been engineered by modifying the dispersion profile for tailoring the spectral properties of the photon sources [25, 65].

Frequency correlated photon sources with a broadband spectrum are important for the deployment of these applications. Recent advances include the generation of these broadband frequency correlated photons using integrated cavities for enhancing the flux of photons in several platforms such as high index doped glass [66], SOI [67, 68], AlGaAs-OI [17, 69], GaN[70], LN [71] and Si_3N_4 [72, 73, 74] .



Figure 4.1: Schematic representation of a frequency comb generated by a single bus microring resonator photon source.

As we mentioned before, Si_3N_4 is considered as an optimal platform for the design of the photonic circuits since it has a larger refractive index, but not too high in comparison with the previous materials mentioned. This allows to engineer the phase matching by properly choosing the appropriate combination of the width and height.

In this chapter, we provide the steps followed to design an integrated photon source by engineering a microring resonator based on a single bus waveguide configuration (see figure 4.1). The photon source generates a quantum frequency comb with a broadband spectrum that covers at least 22.6 THz for 450 frequency correlated modes with 50 GHz mode spacing highly compatible with the DWDM system based on 50 GHz grid in the C-band.

First we analyze and compare the dispersion profile for a waveguide with SiO_2 and air cladding. Afterwards we compare our proposed source with a height of 500 nm with the most recent height of 800 nm which has been recently reported in terms of dispersion and phase-matching. Following this, we compare the flux of photons expected from our proposed photon source and one similar resonator with height of 800 nm, showing enhancement. In addition, we briefly review the fabrication process of our devices and the mask design.

Finally, we describe the measurements performed over the ring resonators as well as the characterization in terms of temperature shifting, Q-factor and integrated dispersion.

4.2 Simulation of a broadband integrated photon source

We start by designing the integrated photon source. To do this, we simulated the effective refractive index using the WMM solver, similarly as it was done in the previous chapter. For this case, we selected as a pump $\lambda_p = 1550$ nm since we target our photon source to produce the broadband frequency correlated modes in the telecom band. To achieve the broadband spectrum, the pump must be in the anomalous dispersion region close to the zero dispersion wavelength. Therefore, we focus on finding a geometry where the dispersion for the pump wavelength is small and close to the ZDW.

4.2.1 Dispersion comparison for silicon dioxide and air cladding

First, we compare and briefly discuss the use of SiO_2 cladding in a waveguide. In figure 4.2 the cross section of a ridge waveguide with different claddings is shown, as well as the width and height of the waveguides. Figure 4.2 a) shows the Si_3N_4 waveguide with air cladding while b) shows the Si_3N_4 waveguide with SiO_2 cladding.

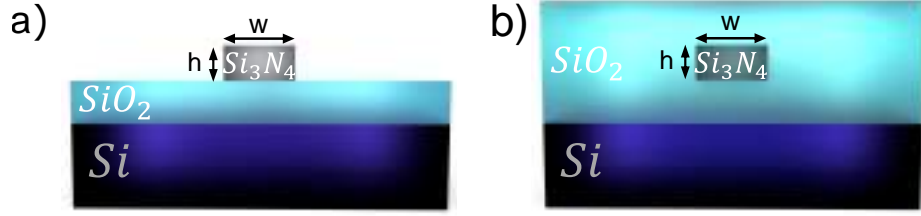


Figure 4.2: Cross section of a Si_3N_4 on insulator ridge waveguide with: a) air cladding and b) SiO_2 cladding.

One advantage in considering air cladding is that the steps involved in the fabrication process are easier in comparison with the SiO_2 cladding in which it is required to deposit an extra layer. Although, this makes the device more unstable and susceptible to environment fluctuations and can be contaminated with dust which will affect the ring performance. Moreover, the effective refractive index will be directly affected. Thus, we simulated both configurations to compare them in terms of the spectral bandwidth generation and photon flux.

First, we analyze the case when the height is fixed at $h = 500$ nm, considering air cladding and SiO_2 cladding. Figure 4.3 a) and b) shows the dispersion for the TE_{00} (solid line) and TM_{00} (dashed line) modes, respectively. In this case the SiO_2 -cladding is denoted by circles in the plots. We include a vertical line at 1550 nm wavelength which helps to find a geometry that crosses with low dispersion.

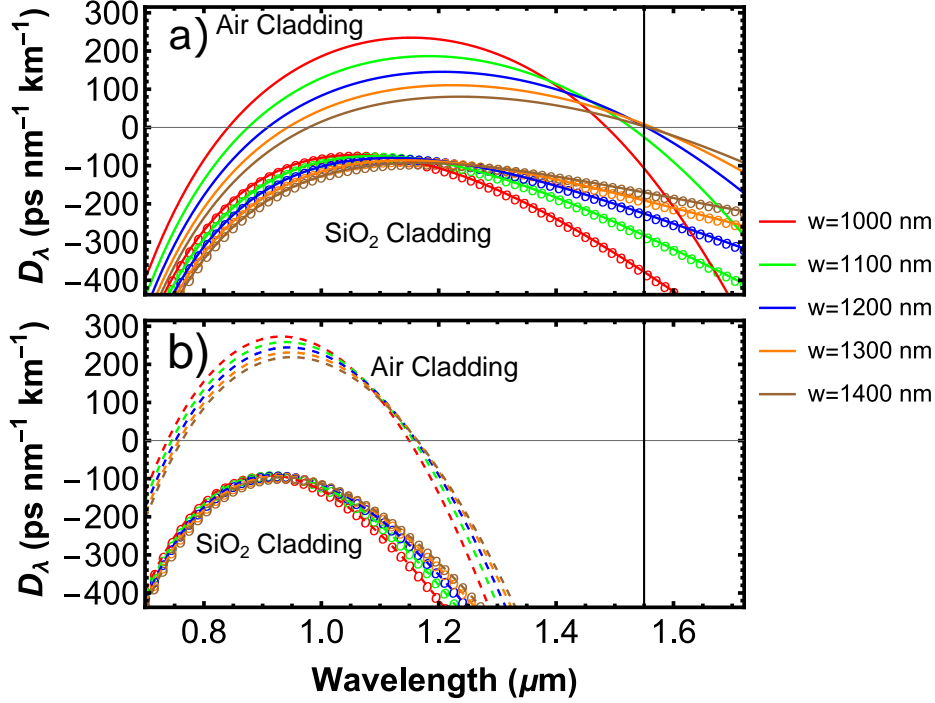


Figure 4.3: Dispersion as a function of the wavelength for a fixed height $h = 500$ nm, considering SiO₂ and air cladding for several widths for: a) the TE₀₀ mode and b) TM₀₀ mode.

For the TE₀₀ mode, we obtain that the dispersion for the waveguide surrounded by SiO₂ is in the normal dispersion for all the wavelengths, while the waveguide surrounded by air is in the anomalous dispersion. Additionally, we observe that for widths bigger than 1200 nm, there is low anomalous dispersion at 1550 nm wavelength.

Similarly for the TM₀₀ mode, we obtain that the waveguide surrounded by SiO₂ is in the normal dispersion for all the wavelengths and, for the waveguide surrounded by air can be in the anomalous dispersion. Nonetheless, for this mode it is not possible to reach anomalous dispersion at 1550 nm wavelength.

We conclude that the use of SiO₂-cladded waveguides are not suitable for our purpose. On the other hand, in recent years the use of Si₃N₄ devices have been reported, with thickness of $h = 800$ nm for nonlinear applications such as integrated photon sources and soliton generation with SiO₂ cladding, since the dispersion profile can be engineered at telecom wavelengths [63, 72, 73].

Then, we compare our proposed waveguides that consists of a thickness of $h = 500$ nm and air cladding with waveguides that consists of a thickness of $h = 800$ nm and SiO₂ cladding. The width has been selected as the only degree of freedom to engineer the dispersion profile.

Figure 4.4 shows in a) the TE_{00} mode (solid line) and in b) the TM_{00} (dashed line) mode for six geometries, in which three of them have a thickness of 500 nm and the three remaining have a thickness of 800 nm.

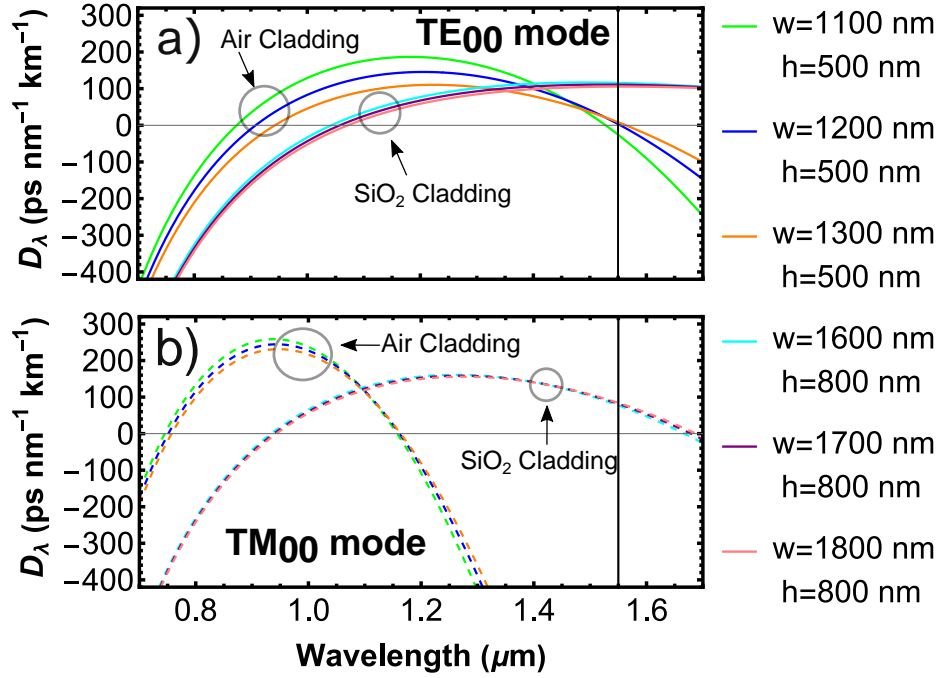


Figure 4.4: Dispersion as a function of the wavelength for two cases: thickness of 500 nm (air cladding) and 800 nm (SiO_2 cladding) for three different widths each one and for: a) the TE_{00} mode and b) TM_{00} mode.

For the TE_{00} mode (figure 4.4 a)), all the waveguides show anomalous dispersion in a broadband spectrum and it can be seen that the dispersion is lower than $300 \text{ ps}/(\text{nm km})$ for all the waveguides. However, the zero dispersion wavelength is expected at larger wavelengths for the thickness of 800 nm (SiO_2 cladding), surpassing 1550 nm. On the other hand, for the TM_{00} mode (figure 4.4 b)), just the waveguides with thickness of $h = 800$ nm show anomalous dispersion at 1550 nm, while the waveguides with thickness of $h = 500$ nm do not reach anomalous dispersion at 1550 nm wavelength since the second ZDW is around 1200 nm.

From these plots we can obtain information about if some geometry is interesting or not. For our case, both configurations seem promising since the dispersion profile for both polarizations is low and in the anomalous region. Nevertheless, some extra properties information is needed to choose the optimal configuration.

4.2.2 SFWM phase-matching condition

In figure 4.5, the contour plots of the phase matching are shown for the six different geometries for the TE_{00} and TM_{00} modes, in terms of the detuning frequency. The vertical line is used to show the frequency/wavelength in which we want to pump our photon source corresponding to $\lambda_p = 1550$ nm.

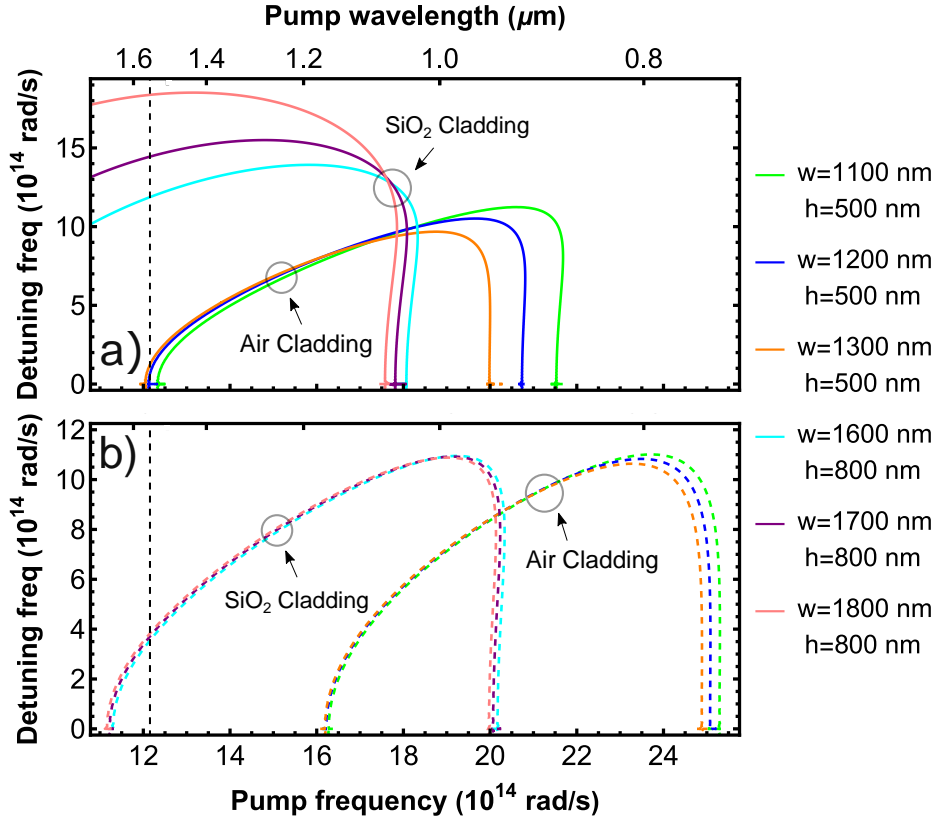


Figure 4.5: Contour plots of the phase-matching condition in terms of the detuning frequency $\Omega_{s,i}$ i.e., $\Delta\beta(\omega) = 0$, for two cases: thickness of 500 nm (air cladding) and 800 nm (SiO_2 cladding) for three different widths each one and for: a) the TE_{00} mode and b) TM_{00} mode.

It can be seen, that for the waveguides with thickness $h = 500$ nm (air cladding, TE_{00} mode) the pump can be reached by the geometry with a small value of detuning ($\Omega_{s,i} \approx 0$). For the waveguides with thickness $h = 800$ nm (SiO_2 cladding, TM_{00} mode) have a phase-matching with a value of detuning ($\Omega_{s,i} \approx 4 \times 10^{14}$ rad/s), which means that the photons will be separated from the pump.

In figure 4.6, the signal and idler wavelengths are shown as a function of the pump wavelength for both modes. For the TE_{00} mode (4.6 a)), the waveguides with SiO_2 have larger wavelengths, which physically are not possible since those wavelengths are

not supported for the waveguides. Besides, for the waveguides with air cladding we identify as candidates the widths 1200 and 1300 nm since we are close to the ZDW. As it was previously mentioned, for the copolarized SFWM, the ZDW corresponds to the wavelength where the photons start to be separated from the pump.

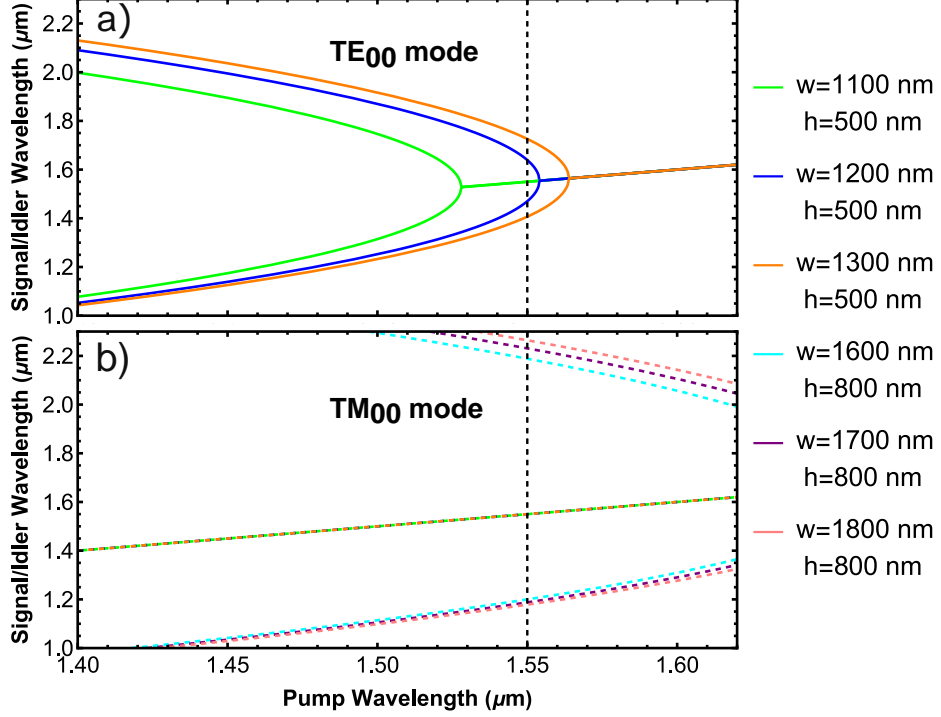


Figure 4.6: Wavelength of the signal and idler photons as a function of the pump wavelength for two cases: thickness of 500 nm (air cladding) and 800 nm (SiO₂ cladding) for three different widths each one and for: a) the TE₀₀ mode and b) TM₀₀ mode.

On the other hand, for the TM₀₀ modes we obtain that for the waveguides with SiO₂ cladding, the signal and idler photons are wide spectrally separated from the pump ($\lambda_i \approx 2.2 \mu\text{m}$, $\lambda_s \approx 1.2 \mu\text{m}$), while for the waveguides with the air cladding, the photons will be expected at the same wavelength as the pump. Since we are tailoring our photon source to produce photons close to the pump to increase the bandwidth of generation, this behavior is not suitable for our purpose for the SiO₂ and air cladded waveguides.

To see the tendency of the bandwidth, we calculate the phase matching function as:

$$|\phi(\lambda)|^2 = \left| \text{sinc} \left(\frac{L}{2} \Delta\beta(\lambda) \right) e^{i\frac{L}{2} \Delta\beta(\lambda)} \right|^2, \quad (4.1)$$

4. BROADBAND FREQUENCY COMB GENERATION BY DISPERSION ENGINEERING

where $\Delta\beta(\lambda) = 2\beta(\lambda_p) - \beta(\lambda) - \beta(\frac{\lambda_p\lambda}{2\lambda - \lambda_p})$, and the pump wavelength is centered at $\lambda_p = 1.55 \mu\text{m}$. Just for comparison purposes, we choose the length of the waveguide as $L = 1 \text{ cm}$. We want to point out, that until this step, no cavity effect was included, which means, we are just considering that the light is propagating in a straight waveguide.

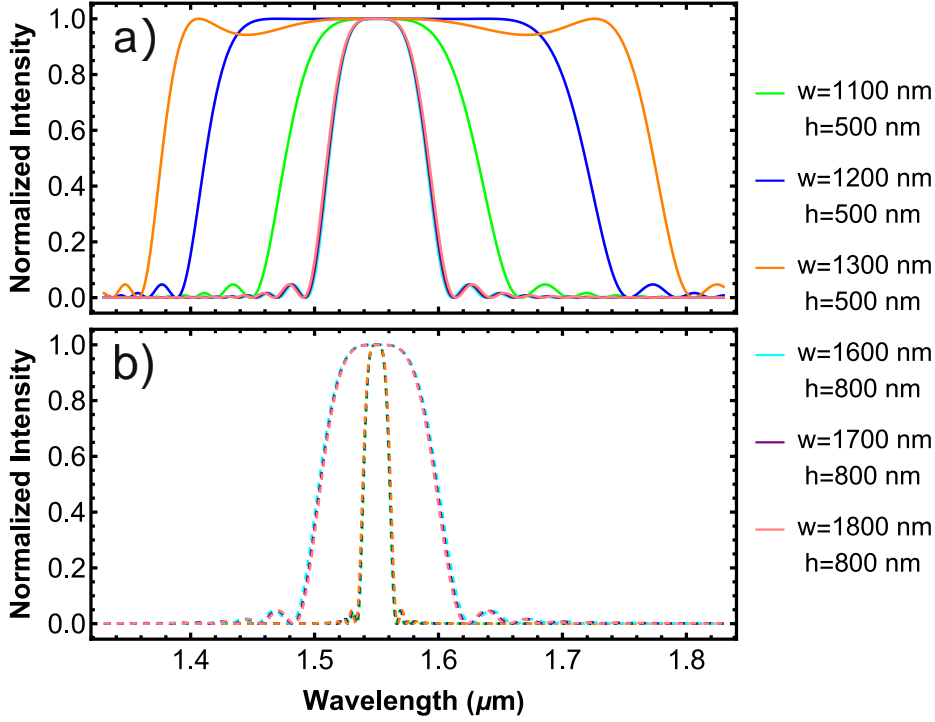


Figure 4.7: Phase-matching a function of the wavelength in a waveguide with 1 cm length and for two cases: thickness of 500 nm (air cladding) and 800 nm (SiO_2 cladding) for three different widths each one and for: a) the TE_{00} mode and b) TM_{00} mode.

Figure 4.7 shows the phase matching function obtained from equation 4.1 for the TE_{00} and TM_{00} modes. First, we analyze the graph for the TM_{00} modes. It can be observed that the three waveguides with air cladding have a similar narrow band spectrum in comparison with the three waveguides with SiO_2 cladding.

On the other hand, for the TE_{00} modes we obtain a similar bandwidth for the three waveguides with SiO_2 cladding but that does not happen for the three remaining waveguides. For the air cladded waveguides at $\lambda_p = 1550 \text{ nm}$, the width $w = 1100 \text{ nm}$ is in the normal dispersion region, giving a bandwidth smaller in comparison with $w = 1200 \text{ nm}$ and $w = 1300 \text{ nm}$. Therefore, by looking at the bandwidth obtained by these two geometries we can obtain a large number of frequency correlated photon pairs after including the cavity effect, therefore we choose the optimal geometry for our purpose $w = 1300 \text{ nm}$ and $h = 500 \text{ nm}$.

The next step after we identify a suitable geometry is to include the cavity effect and determine the final bandwidth and flux of photons that our photon source can produce. For comparison purposes, we estimate these properties for a resonator with a thick cross section with $w = 1700$ nm and $h = 800$ nm and our resonator with $w = 1300$ nm and $h = 500$ nm, both configurations are just simulated with the TE₀₀ polarization.

4.2.3 Cavity effect in the SFWM process

We proposed a photon source highly compatible with current telecom technologies. We target the photon source to provide a frequency comb with $FSR_\nu = 50$ GHz spacing. Then, we determine through equation 2.22, that the radius of the ring must be $R = 440$ μm to provide this specific FSR.

As it was mentioned before, the resonances are determined by the resonance condition $\beta L = 2\pi l$. This means that the resonances are discrete specific frequencies that satisfies equation 2.20. As a brief reminder, higher frequencies from the pump are used to describe the signal photons, while lower frequencies from the pump are used to describe the idler photons.

Therefore, we determine the frequencies of the resonances of the cavity through the equation $\omega_l = lc(Rn_{\text{eff}})^{-1}$. Then, the pump frequency is determined by $\omega_p = l_p c(Rn_{\text{eff}})^{-1}$. In accordance with the previous description of the signal and idler frequencies, it is customary to employ the mode index notation in which $\mu = 0$ denotes the mode of the pump. Accordingly, the signal and idler modes are described by:

$$\begin{cases} \mu_s = l - l_p & \omega > \omega_p \\ \mu_i = l - l_p & \omega < \omega_p \end{cases} \quad (4.2)$$

On the other hand, the Q-factor and the radius appear in the matrix $\mathcal{M}_{cav}(\nu_s, \nu_i)$ which is written in terms of the Airy functions mentioned in the theoretical chapter 2. To show the effect of the matrix $\mathcal{M}_{cav}(\nu_s, \nu_i)$, in figure 4.8 the plots of the matrix for three different Q-factors are shown.

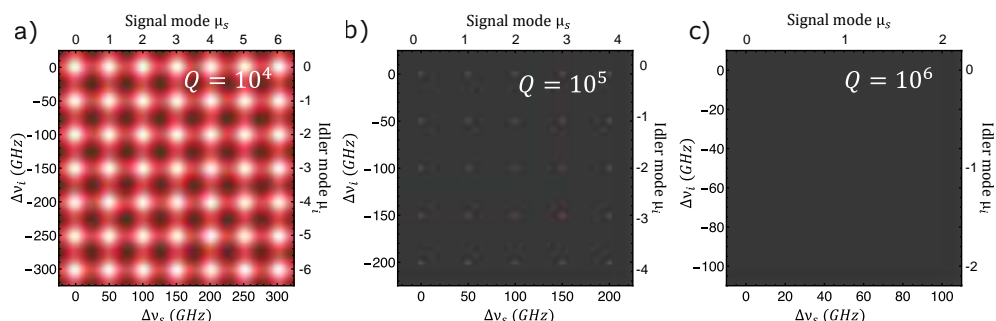


Figure 4.8: Cavity function $\mathcal{M}_{cav}(\nu_s, \nu_i)$ where it is clearly visible how the resonances become narrower when increasing the Q-factor for a) $Q = 10^4$, b) $Q = 10^5$ and c) $Q = 10^6$.

4. BROADBAND FREQUENCY COMB GENERATION BY DISPERSION ENGINEERING

We want to point out that figure 4.8 shows the matrix $\mathcal{M}_{cav}(\nu_s, \nu_i)$ for our proposed photon source with $w = 1300$ nm, $h = 500$ nm and $R = 440$ μm . Note that the spacing between resonances is 50 GHz corresponding to the FSR of the resonator. Moreover, note that for the Q-factor $Q = 10^4$, the resonances are wide and are connecting with neighbor resonances, while for $Q = 10^5$ and $Q = 10^6$, it is clearly visible how the resonances become sharper and narrower, leading to not interacting with neighbor resonances when the Q-factor is increased. A similar behavior is expected for a resonator with the SiO₂ cladding ($w = 1700$ nm, $h = 800$ nm).

The final step in our design process is to include the cavity effect to the SFWM process and estimate the final bandwidth of the photons generated in both photon sources. First we obtained the effective area of both waveguides. In figure 4.9 the norm of the electric field distribution for the TE₀₀ mode is shown, for: a) our proposed photon source $w = 1300$ nm, $h = 500$ nm with air cladding and b) thick waveguide for comparison with $w = 1700$ nm, $h = 800$ nm with SiO₂ cladding. It can be seen that the effective area is lower for the waveguide air cladded, this will affects directly the photon flux which is inversely proportional to A_{eff} .

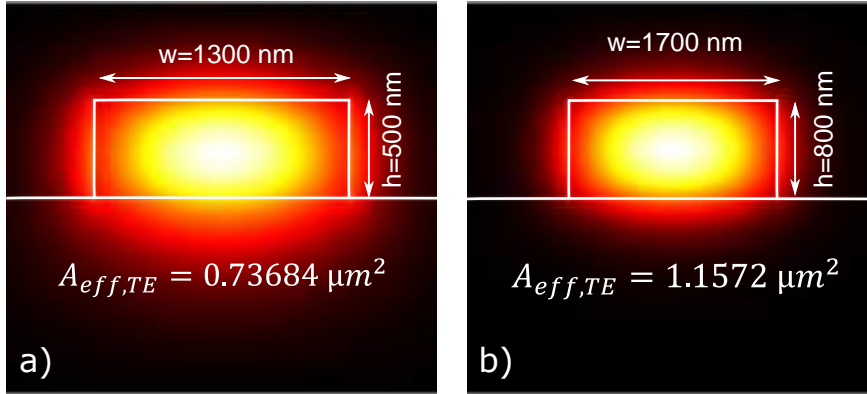


Figure 4.9: Norm of the electric field distribution of the TE₀₀ mode with the respective effective area for a) 1300 nm width and 500 nm height and b) 1700 nm width and 800 nm height.

In table 4.1 the full parameters are shown for both geometries as a summary.

Top cladding	Cross section (nm×nm)	Radius(μm)	FSR_ν (GHz)	$A_{eff,TE}(\mu\text{m}^2)$
Air	$w = 1300, h = 500$	440	50.2	0.7368
SiO ₂	$w = 1700, h = 800$	440	51.2	1.1572

Table 4.1: Summary of the parameters for the resonator considering the TE₀₀ mode.

For the calculation of the SiO₂ resonator, we selected the same radius, where we obtained just 1 GHz difference in the FSR_ν mainly due to the geometry of the waveg-

uide and, consequently, the effective refractive index. Despite this, we obtained a big difference in the effective area which will affect the flux of photons as it is inversely proportional to the effective area. Hence a smaller effective area will increase the flux of photons.

4.2.4 Frequency comb and flux of photons

On the other hand, we calculated the full JSI with a theoretical Q-factor $Q = 10^5$ that can be easily achievable at telecom wavelengths, and considering a CW laser centered at $\lambda_p = 1550$ nm with a narrow linewidth $\delta\nu_p = 200$ kHz. This allows us to compare the performance of both configurations for the two ring resonators presented in the previous section.

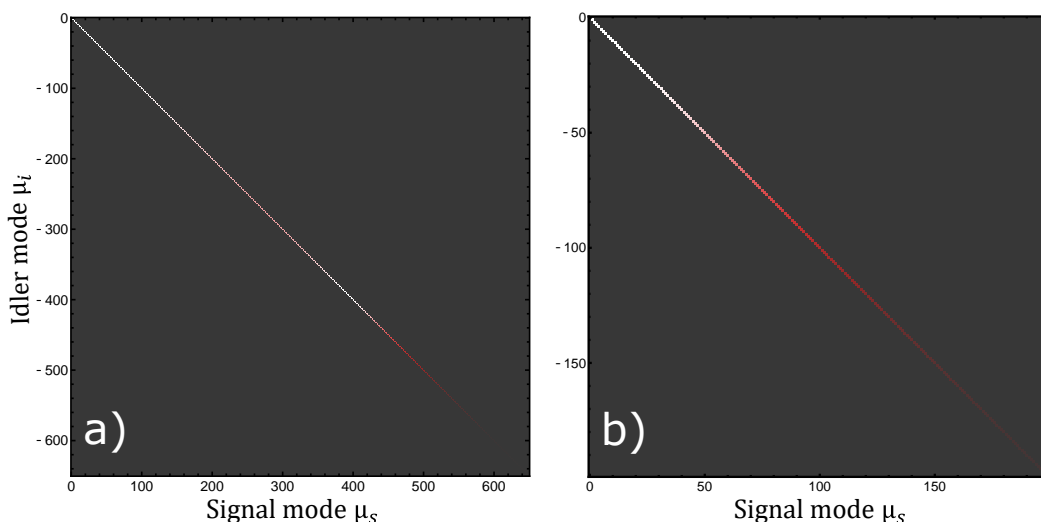


Figure 4.10: Simulation of the normalized Joint Spectral Intensity for the two different configurations of ring resonators. a) Frequency comb generated by the ring with width 1300 nm and 500 nm height, and b) frequency comb generated by the ring with width 1700 nm and 800 nm height.

In figure 4.10 the full normalized JSI for the frequency correlated modes are shown. Figure 4.10 a) corresponds to our proposed ring resonator ($w = 1300$ nm, $h = 500$ nm with air cladding), which shows the frequency comb extends near to 450 frequency correlated modes. Figure 4.10 b) shows the frequency comb for the thick geometry with the SiO₂ cladding, in which, the frequency correlated modes are close to 74 modes (estimated at FWHM). Note that only the terms over the main diagonal are different from zero, while the off-diagonal terms are zero. This can be explained by the narrow linewidth of the CW laser used as a pump, which only excites the modes along the main diagonal and not those spaced by multiples of the FSR ($\delta\nu_p < FSR$).

4. BROADBAND FREQUENCY COMB GENERATION BY DISPERSION ENGINEERING

Finally, we estimated the flux of photons of both ring resonators through the use of equation 3.7:

$$N_{cw} = \frac{2^5 c^2 n_{eff}^2(\omega_p) L^2 \gamma^2 P_0^2}{\pi \omega_p^2} \int d\omega \frac{\omega(2\omega_p - \omega) \beta'(\omega) \beta'(2\omega_p - \omega)}{n_{eff}^2(\omega) n_{eff}^2(2\omega_p - \omega)} \times \mathcal{M}_{cav}(\omega, 2\omega_p - \omega) \text{sinc}^2 \left(\frac{L \Delta \beta_{cw}}{2} \right). \quad (4.3)$$

In this case, every mode is integrated into a window of 20 GHz. Figure 4.11 shows the flux of photons for both configurations, where the cavity effect is already included.

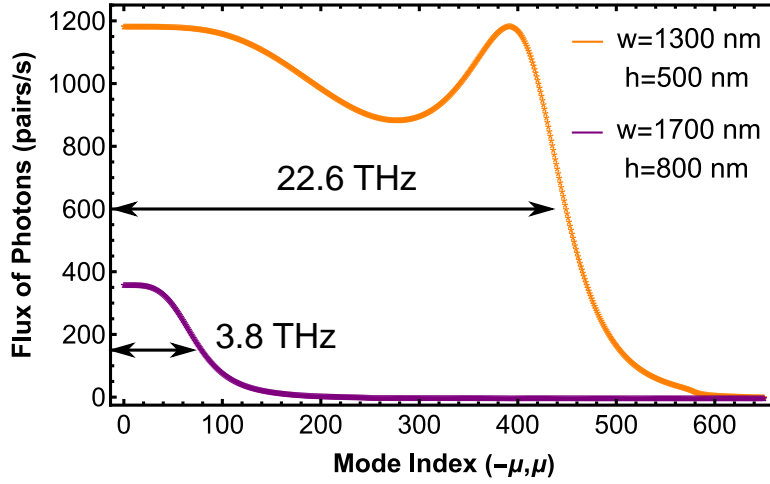


Figure 4.11: Simulated flux of photons for the correlated modes for the two different configurations of ring resonators.

We obtain that for the resonator with SiO₂ cladding, $w = 1700$ nm and $h = 800$ nm is capable to produce a maximum of 362 pairs/s, where the bandwidth is determined at FWHM giving 74 frequency correlated modes that covers 3.8 THz of correlated photon pairs.

In contrast, our proposed photon source with air cladding, $w = 1300$ nm and $h = 500$ nm can produce 22.6 THz of broadband photon pairs, which corresponds to 450 frequency correlated modes with a maximum of 1185 pairs/s.

Note that the flux of photons for the resonator with air cladding is 3.2 times higher than for the ring with SiO₂ cladding. This is attributed to the difference of the effective refractive index which is higher for the resonator with SiO₂. Moreover, the effective area is bigger for the SiO₂ resonator.

4.3 Fabrication and characterization of integrated microring resonators.

Since the previous design seems suitable for its implementation, we proceeded with the fabrication and characterization the devices. The fabrication was performed at the Université de Technologie de Troyes in Troyes, France, by Mauricio Gomez and Rafael Salas. Furthermore, all the measurements presented in this chapter were performed in the Leibniz Universitat Hannover in Hannover, Germany, in the group of research of Michael Kues.

Figure 4.12 shows the schematic representation of the full process of manufacture by Electron Beam Lithography (EBL).

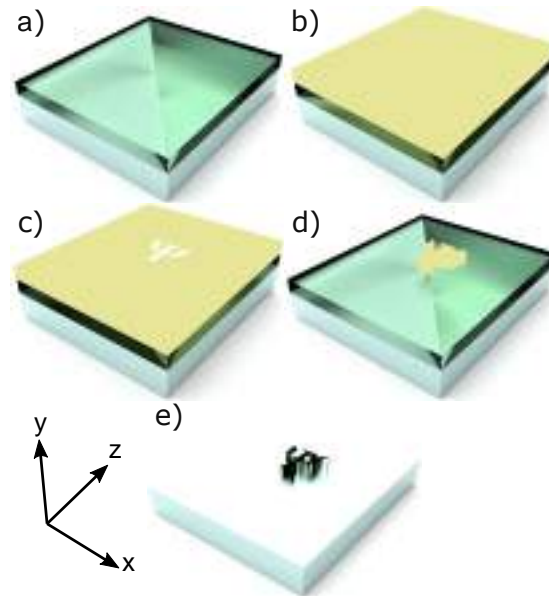


Figure 4.12: Schematic representation of the full process of electron beam lithography for the nanofabrication of nanostructures: a) The sample with a thin film of Si_3N_4 , b) deposition of the e-beam resist with spin coating technique, c) pattern exposure to the electron beam, d) development of the sample to remove the exposed resist and e) reactive ion etching process for the transfer of the pattern to the Si_3N_4 thin film.

The full process is described in [24]. A brief description of the fabrication is described as follows:

The samples consist of a layer of stoichiometric Si_3N_4 (LPCVD deposition) of thickness 500 nm placed on top of a SiO_2 layer of 2 μm on top of a Si substrate from University Wafer. Then the e-beam resist is deposited with the use of the spin-coating technique. The resist reacts to the electron beam, then, the pattern is generated and placed, such that the electron beam is focused on the top surface of the resist for the

writing process. After exposure, the sample is developed to remove the unexposed resist and finally, the pattern is transferred to the Si_3N_4 with the use of reactive ion etching technique.

4.3.1 GDSII file

To create the integrated microring resonators, we must first generate a pattern that will be transferred to the sample throughout the entire fabrication process outlined below. We used GDS Helpers to design the integrated microring resonators [75]. This is an open source tool and offers many basic structures for the creation of integrated photonic circuits with different level of complexity, depending on the requirements of every user. The structures are created using python libraries and then generated a GDSII file, which is used by the EBL system to transfer the pattern into the resist.

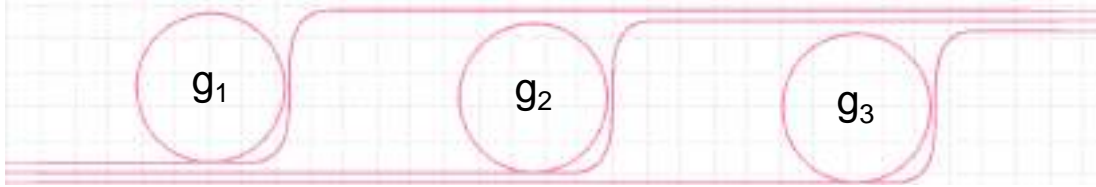


Figure 4.13: GDSII designs of the integrated photon source. The three different rings with the three different gaps are shown.

We designed two samples with the following devices: the first sample has three microring resonators where the bus waveguide and the ring resonator have a cross section of $w = 1300$ nm, $h = 500$ nm with a fixed radius $R = 440$ μm , for three different gaps: $g_1 = 400$ nm, $g_2 = 600$ nm and $g_3 = 800$ nm. Additionally, a second sample was fabricated after analyzing the results obtained from the first sample. The second sample has four rings with the same radius but gaps $g_1 = 350$ nm, $g_2 = 400$ nm, $g_3 = 450$ nm and $g_4 = 500$ nm. Figure 4.13 shows the final image of the devices for the first sample generated with GDS helpers library.

It is important to note that, our samples are too thin, which can be challenging for coupling light to the chip with common fibers or fiber lenses. To overcome this concern, SU8 mode converters are used. The SU8 ($n \approx 1.45$) waveguides have a cross section of 3×3 μm^2 that can match to efficiently couple to a fiber lens or SMF-28 fibers. Then the SU8 waveguides are placed on top of the Si_3N_4 waveguides, where the Si_3N_4 waveguides are tapered down to 200 nm to expand the mode field diameter and increase the coupling from the SU8 waveguide to the Si_3N_4 waveguide.

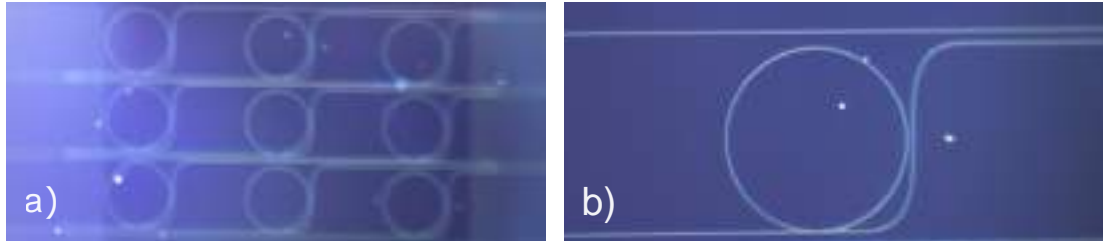


Figure 4.14: Microscope images of the first sample of ring resonators.

In figure 4.14, microscope images of the ring resonators (first sample) as a final result of the full fabrication process are shown. Some small particles and dust can be clearly seen, which can affect the performance of the photonic chip.

4.3.2 Transmission spectra measurements

After the samples were fabricated, we performed a classical characterization of the performance of the devices. Figure 4.15 shows the schematic representation of the setup implemented.

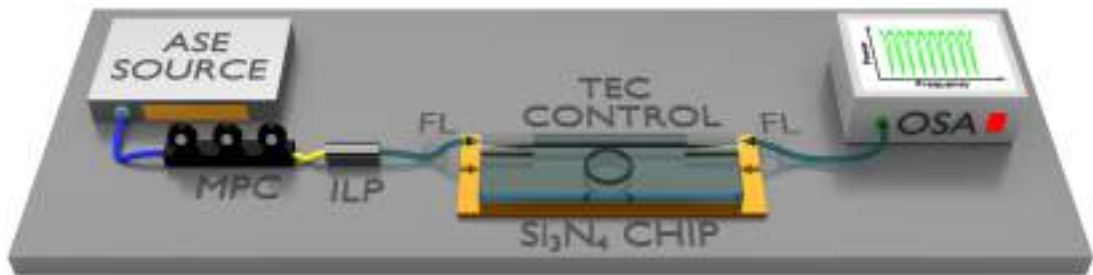


Figure 4.15: Schematic representation of the setup used to characterize and measure the ring resonators.

Before coupling to the photonic chip, a calibration step was performed which consisted in finding the vertical and horizontal polarization in the input and output fiber lens (FL). Then, an Erbium Doped Fiber Amplifier (EDFA) is used as an Amplified Spontaneous Emission (ASE) source which provides a broadband spectrum that is used to pump the resonators. An In-Line Polarizer (ILP) is used to filter the slow-axis polarization. Hence, the polarization from the source is optimized with the Manual Polarization Controllers (MPC) to achieve the maximum power. A second fiber lens is used to out coupling the light from the chip and then is sent to an optical spectrum analyzer to measure the spectrum.

Furthermore, the microring resonators are placed on top of a temperature controller to keep them stable.

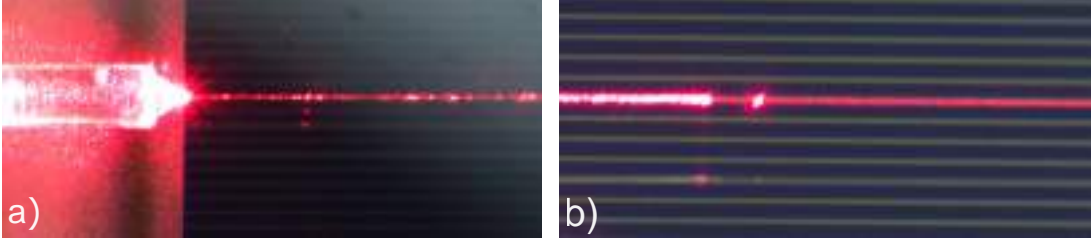


Figure 4.16: Microscope images for the coupling and outcoupling of light in the micro ring resonator. a) Fiber lens used to couple light to the photonic chip and b) output of the chip in the Si_3N_4 taper and the SU8 waveguide.

Figure 4.16 a) shows a microscope image where we can see the light coupling from the fiber lens to the photonic chip through the SU8 waveguide, while in b) shows the light coming at the output of the chip, where it can be clearly seen that the light coupled from the tapered Si_3N_4 waveguide to the SU8 waveguide.

4.3.3 Sample 1

The sample 1 consists of three microring resonators, each with a constant radius of $R = 440 \mu\text{m}$. The only varying parameter is the gap, which takes values of $g_1 = 400 \text{ nm}$, $g_2 = 600 \text{ nm}$ and $g_3 = 800 \text{ nm}$. To characterize them, we measured both polarization states which is selected before the photonic chip.

4.3.3.1 TE polarization

First we prepared $|H\rangle$ polarization with the first fiber lens to excite the TE_{00} mode. Figure 4.17 a) shows the normalized transmission spectrum measured for the three different microring resonators. The resonance peaks does not appear in the same frequencies for the gaps $g_1 = 400 \text{ nm}$ and $g_2 = 600 \text{ nm}$ and are slightly shifted, this is attributed to errors in the fabrication process. Moreover, we measured the $FSR_{\nu,TE} = 51.3 \text{ GHz}$ giving a good agreement with the design.

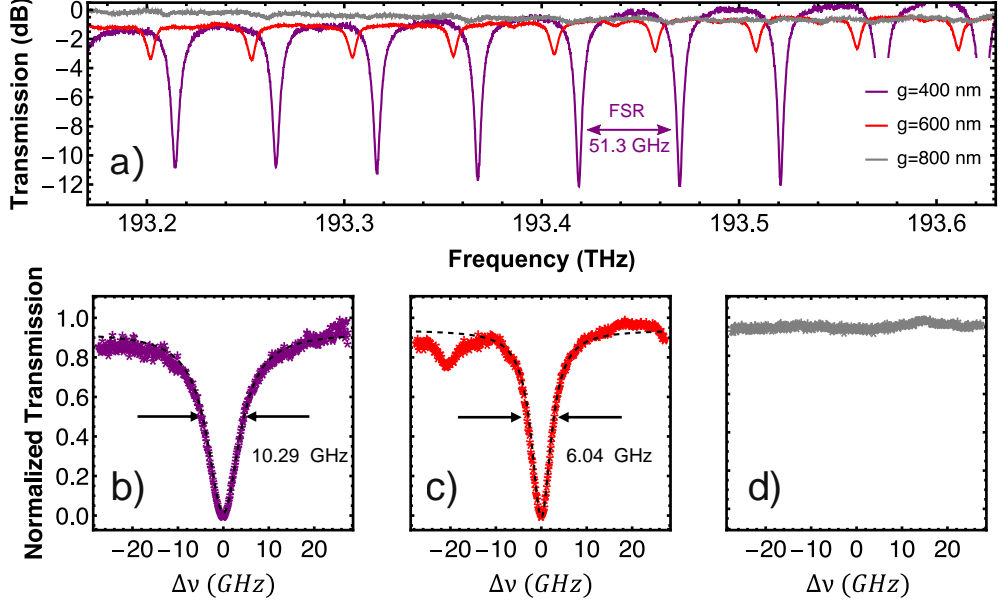


Figure 4.17: a) Normalized transmission spectra measured for different gaps of a ring resonator for the TE_{00} mode. Resonance dips for different gaps and fitted to a Lorentzian function extracting the bandwidth at FWHM, b) $g = 400$ nm with a bandwidth $\Delta\nu = 10.29$ GHz, c) $g = 600$ nm with a bandwidth $\Delta\nu = 6.04$ GHz and d) no resonance dip identified which shows the bus waveguide is not interacting with the resonator.

We observe for the gap $g_3 = 800$ nm, that there are no peaks, which means that the light is not coupled to the resonator. From the spectra, we choose the peaks closest to 193.4 THz (1550.12 nm) to obtain the bandwidth of the resonances. We normalized and fitted the peaks to a Lorentzian function of the form:

$$f(\nu) = A \frac{\Gamma}{(\nu_0 - \nu)^2 + \Gamma^2}, \quad (4.4)$$

where ν_0 represents the center of the peak, A and Γ are related to the amplitude and the width of the peaks, respectively. Furthermore, through the bandwidth of the resonance we calculate the Q-factor as $Q = \nu_0/\Delta\nu$.

From the fit, we obtain that the gap $g_1 = 400$ nm (figure 4.17 b)) has a bandwidth of $\Delta\nu_1 = 10.29$ GHz which gives a Q-factor $Q_1 = 1.8 \times 10^4$. While for the gap $g_2 = 600$ nm (figure 4.17 c)), we estimate a bandwidth $\Delta\nu_2 = 6.04$ GHz which gives $Q_2 = 3.19 \times 10^4$.

In addition, we extracted the peaks locations of the spectrum corresponding for the two different ring resonators and calculated the integrated dispersion for the TE_{00} mode.

4. BROADBAND FREQUENCY COMB GENERATION BY DISPERSION ENGINEERING

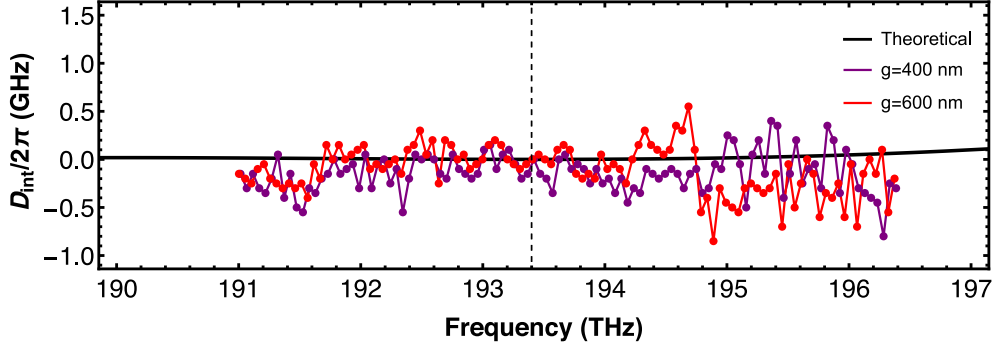


Figure 4.18: Integrated dispersion as a function of the frequency for the TE_{00} mode. The theoretical value of the integrated dispersion is shown as the black line, while the dots correspond to the peaks measured from the transmission spectra for all the rings of the sample 1.

Figure 4.18 shows the integrated dispersion as a function of frequency. The black line corresponds to the theoretical integrated dispersion obtained from the simulations while the different color dots correspond to the measured peaks. Note that for the last gap it is not possible to obtain the resonant frequencies and in consequence, the integrated dispersion can not be determined.

4.3.3.2 Temperature shifting for the TE mode

On the other hand, we measured the spectrum when the temperature is changed with the TEC system. We swept the temperature from 22.36 °C to 24.06 °C with step of 0.1 °C.

In figure 4.19 the normalized transmission spectra is shown, where the resonances shifting can be seen in terms of the temperature, we observe that the resonances shift to higher frequencies.

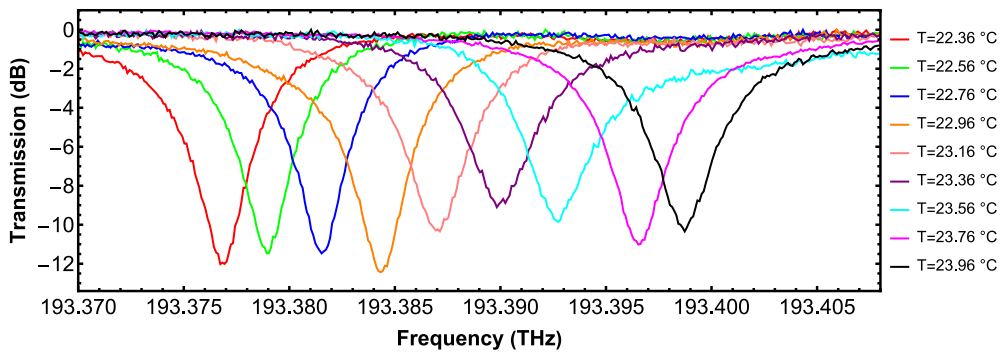


Figure 4.19: Normalized transmission spectra measured for a ring resonator for the TE_{00} mode with different temperatures showing the shifting.

We obtained from the previous transmission spectra the peaks locations in terms of the temperature and fitted the peaks. We find that the peak shifting follows a straight line, with the slope of the line indicating the resolution of the resonator in terms of the temperature.

Figure 4.20 a) shows the peaks frequency difference as a function of the temperature difference where the slope of the fit corresponds to $\frac{\Delta\nu}{\Delta T} = 14.15 \text{ GHz}/^\circ\text{C}$.

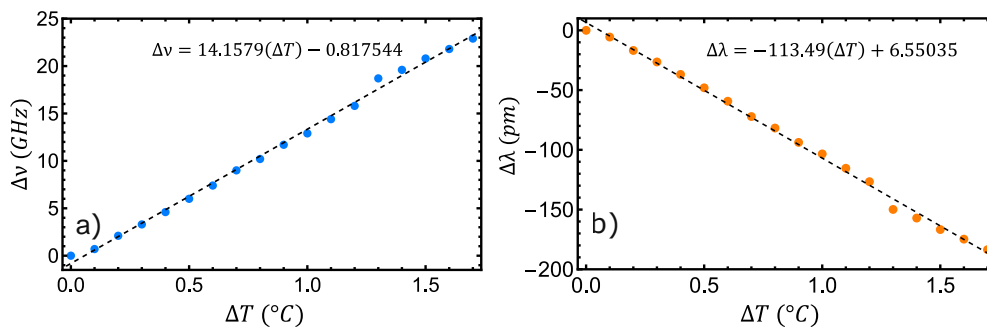


Figure 4.20: Shifting of the peaks taken from the previous spectra and their corresponding fittings as a function of the temperature written in: a) frequency detuning and b) wavelength detuning.

Typically, the shifting of the peaks is written in terms of the wavelength, figure 4.20 b) shows the wavelength difference shifting as a function of the temperature difference where the slope of the fit corresponds to $\frac{\Delta\lambda}{\Delta T} = -113.49 \text{ pm}/^\circ\text{C}$. The sign of the shift indicated that the peaks are moving to shorter wavelengths.

4.3.3.3 TM polarization

Although we targeted our photon source to work with the TE polarization, we measured the spectra of the TM polarization for sample 1 to fully characterize the chip and compare the results theoretically.

4. BROADBAND FREQUENCY COMB GENERATION BY DISPERSION ENGINEERING

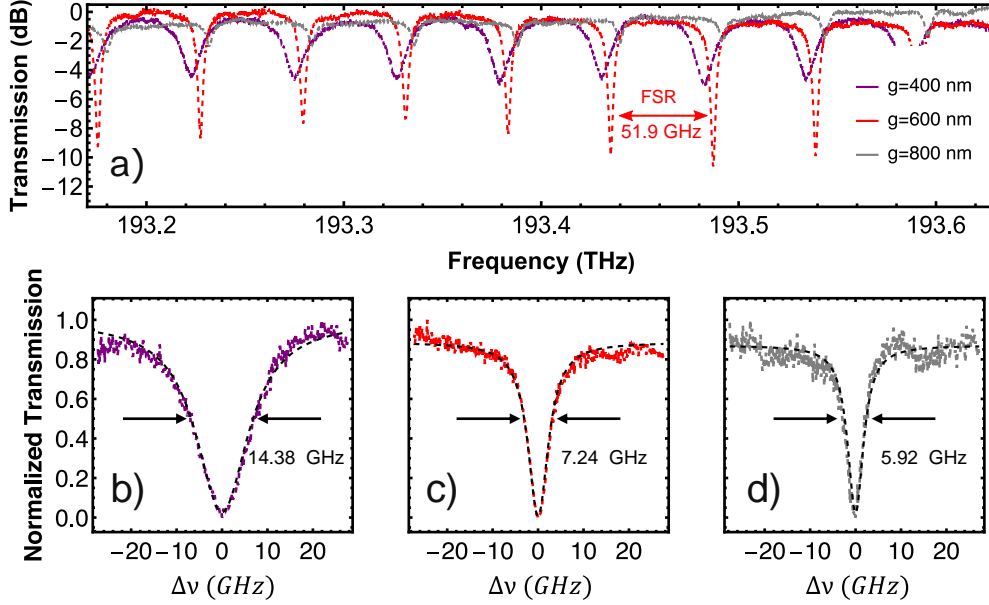


Figure 4.21: a) Normalized transmission spectra measured for different gaps of a ring resonator for the TM_{00} mode. Resonance dips for different gaps and fitted to a Lorentzian function extracting the bandwidth at FWHM, b) $g = 400$ nm with a bandwidth $\Delta\nu = 14.38$ GHz, c) $g = 600$ nm with a bandwidth $\Delta\nu = 7.24$ GHz and d) $g = 800$ nm with a bandwidth $\Delta\nu = 5.92$ GHz.

We achieved this by preparing the $|V\rangle$ polarization with the first fiber lens to excite the TM_{00} mode. Figure 4.21 a) shows the normalized transmission spectrum measured for the three different microring resonators. As well as for the TE_{00} mode, we obtained a small difference in the peaks location for the gaps $g_1 = 400$ nm, $g_2 = 600$ nm and $g_3 = 800$ nm, which is attributed to errors in the fabrication process. Moreover, we measured the $FSR_{\nu, TM} = 52$ GHz.

In a similar way, we select the resonances closest to 193.4 THz. We normalized the resonance and fitted anew to a Lorentzian function. In figure 4.21 a) the spectra for the three different gaps are shown. The resonance for the gap g_1 (4.21 b)) gives a resonance bandwidth $\Delta\nu_1 = 14.38$ GHz which corresponds to $Q_1 = 1.35 \times 10^4$. For the second gap (4.21 c)), we obtained a bandwidth $\Delta\nu_2 = 7.24$ GHz that provides a Q-factor $Q_2 = 2.66 \times 10^4$ and finally, for the largest gap (4.21 d)) we obtain a bandwidth $\Delta\nu_3 = 5.92$ GHz giving a Q-factor $Q_3 = 3.26 \times 10^4$. In contrast to the TE_{00} mode, we observe that for the gap $g_3 = 800$ nm, still existing coupling from the bus waveguide to the microring resonator.

Moreover, we obtained the peaks locations of the spectrum corresponding for the three different ring resonators and calculated the integrated dispersion for the TM_{00} mode.

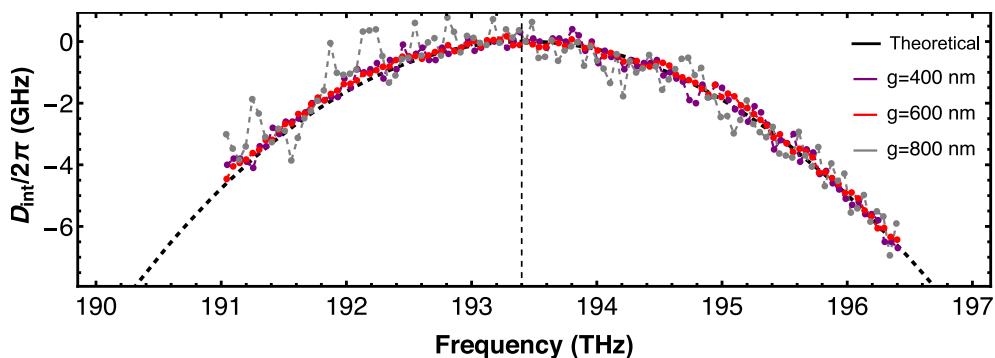


Figure 4.22: Integrated dispersion as a function of the frequency for the TM_{00} mode. The theoretical value of the integrated dispersion is shown as the black dashed line, while the dots correspond to the peaks measured from the transmission spectra for all the rings of the sample 1.

Figure 4.22 shows the integrated dispersion as a function of frequency. The black dashed line corresponds to the theoretical integrated dispersion obtained from the simulations while the different color dots correspond to the measured peaks. It can be clearly seen that the tendency of the integrated dispersion is different in comparison with the TE mode, this allows us to discriminate as well for the different polarizations of the microring resonators.

4.3.4 Sample 2

In addition, a second sample was fabricated and characterized only for the TE_{00} mode. This sample consists of four microring resonators with the same dimensions as the bus waveguide and the microring resonator, with the difference that we choose four different gaps $g_1 = 350$ nm, $g_2 = 400$ nm, $g_3 = 450$ nm, and $g_4 = 500$ nm.

4. BROADBAND FREQUENCY COMB GENERATION BY DISPERSION ENGINEERING

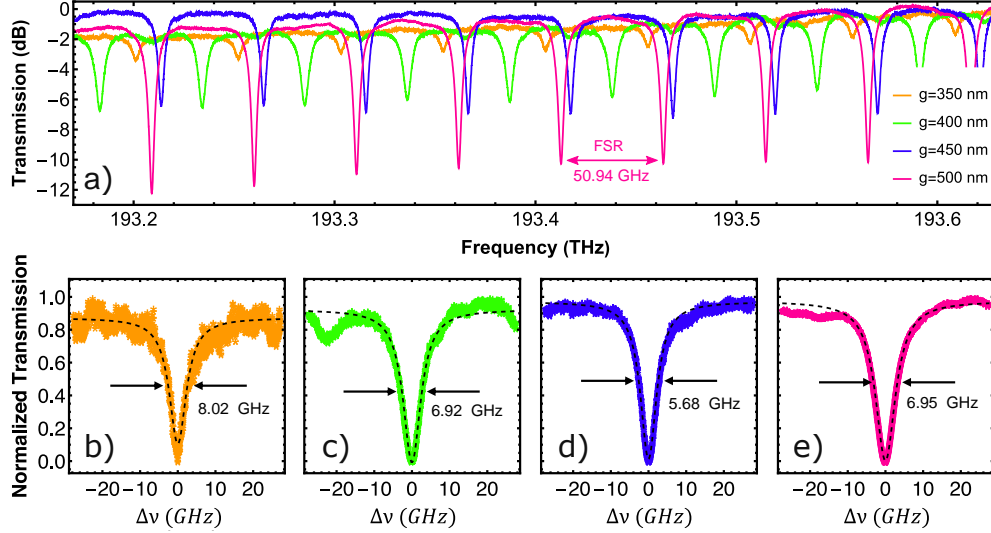


Figure 4.23: a) Normalized transmission spectra measured for different gaps of a ring resonator for the TE_{00} mode. Resonance dips for different gaps and fitted to a Lorentzian function extracting the bandwidth at FWHM, b) $g = 350$ nm with a bandwidth $\Delta\nu = 8.02$ GHz, c) $g = 400$ nm with a bandwidth $\Delta\nu = 6.92$ GHz, d) $g = 450$ nm with a bandwidth $\Delta\nu = 5.68$ GHz and e) $g = 500$ nm with a bandwidth $\Delta\nu = 6.95$ GHz.

Figure 4.23 shows the normalized transmission spectrum measured for the four different gaps where the FSR corresponds to 50 GHz as expected. We repeated the process and we selected the resonances closest to 193.4 THz. We normalized the resonance and fitted it again to a Lorentzian function. Figure 4.23 a) shows the resonance for the gap g_1 giving a bandwidth of the resonance $\Delta\nu_1 = 8.02$ GHz which corresponds to $Q_1 = 2.41 \times 10^4$, for the second gap (4.23 b)), we obtained a bandwidth $\Delta\nu_2 = 6.92$ GHz that provides a Q-factor $Q_2 = 2.79 \times 10^4$. For the third gap (4.23 c)), we obtained a bandwidth $\Delta\nu_3 = 5.68$ GHz that provides a Q-factor $Q_3 = 3.4 \times 10^4$ and finally, for the largest gap (4.23 d)) we obtain a bandwidth $\Delta\nu_4 = 6.95$ GHz giving a Q-factor $Q_4 = 2.78 \times 10^4$. Note that when the bandwidth of the resonances becomes narrower, the Q-factor increases. From these results we can infer that the higher Q-factor is expected for gaps between 400 and 500 nm.

Finally, we extracted the peaks locations of the spectrum corresponding for the four different ring resonators and calculated the integrated dispersion.

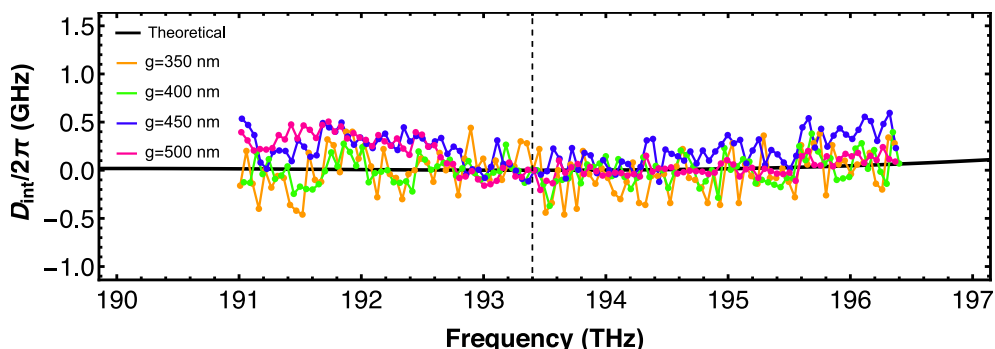


Figure 4.24: Integrated dispersion as a function of the frequency. The theoretical value of the integrated dispersion is shown as the black line, while the dots correspond to the peaks measured from the transmission spectra for all the rings of the sample 2.

Figure 4.24 shows the integrated dispersion as a function of frequency. The black line corresponds to the theoretical integrated dispersion obtained from the simulations, while the different color dots correspond to the measurement for the four different gaps for the sample 2. We observe that the theoretical model is in good agreement with the results, as there is a clear tendency for the measured peaks to align with the theoretical model, with less than a 0.5 GHz difference between the peaks and the model.

Table 4.2 shows the FSR and Q factors of the TE_{00} and TM_{00} modes. The theoretical FSR for the TE_{00} and TM_{00} modes are 50.2 GHz and 50.6 GHz, respectively. We obtain that we have a difference from the theoretical expected values of 1 GHz, we consider this difference is linked to an error in the fabrication process in the width of the microring resonator, which must be corrected in future fabrications.

gap (nm)	$FSR_{\nu,TE}$ (GHz)	$Q_{TE_{00}}$ (1×10^4)	$FSR_{\nu,TM}$ (GHz)	$Q_{TM_{00}}$ (1×10^4)
350 (sample 2)	50.7	2.41	-	-
400 (sample 1)	51.3	1.8	51.6	1.35
400 (sample 2)	51.24	2.79	-	-
450 (sample 2)	51.06	3.4	-	-
500 (sample 2)	50.94	2.78	-	-
600 (sample 1)	51.1	3.19	51.9	2.66
800 (sample 1)	NC	NC	52	3.26

Table 4.2: Summary of the measured parameters for both samples and different gaps in the microring resonators.

From the previous table we can only compare the FSR and Q-factor for the resonator with a gap of 400 nm. For the FSR we obtained only a small difference of 0.06 GHz, that is attributed to small variations in the geometry of the integrated cavity. On the other hand, we obtained an improvement in the Q-factor of $Q = 0.61 \times 10^4$, this represents an

improvement in the quality of the fabrication process between both samples. However, further modifications needs to be addressed such that the Q-factor improves.

4.4 Conclusion

This chapter presents an overview of the detailed process for designing an integrated photon source custom-designed to produce a broadband frequency comb, optimized for compatibility with a 50 GHz grid DWDM telecom system. This is achieved by carefully engineering the dispersion profile of the waveguide and the ring resonator.

We presented a detailed comparison of the use of a top cladding considering air or SiO₂ for several widths where the dispersion can be tuned. In addition, we showed the frequency correlated bandwidth generation expected in the cavity absence and when considering the cavity effect provided by the resonator and the photon flux expected.

Furthermore, a brief review of the fabrication process of the samples is outlined. We show the setup used to characterize the fabricated resonators and the measurements obtained for seven rings in total. The measurements consisted in the estimation of the FSR, Q-factors, for both, TE₀₀ and TM₀₀ modes, and the integrated dispersion and temperature shifting for the TE₀₀ mode.

Finally, these results shows that our proposed photon source is capable of generating up to 450 with 22.6 THz of frequency correlated photon pairs, with a higher flux of photons by using air cladding devices in comparison with SiO₂ cladded devices. This can enable for next generation integrated photon sources with a broadband bandwidth and high brilliance.

Conclusions

In the present thesis, microring resonators in Si_3N_4 were investigated for their potential applications in photonic quantum technologies. Our interest focus in the interesting properties of this material such as high refractive index, transparency window and high nonlinearity that on recent years has been of attraction for photonic quantum circuits.

In particular, our main goal is to explore Si_3N_4 material that allows the design of integrated photon sources by dispersion engineering for two important applications.

- An integrated photon source compatible with a quantum memory.

We performed our analysis to find the geometrical parameters of an integrated photon source capable of producing photons compatible with a quantum memory based on a $\text{Pr}^{3+}:\text{Y}_2\text{SiO}_5$ crystal.

First, we simulated optical waveguides through the WMM solver which is an open source software that allows to obtain the guides modes in the optical waveguides for the two polarizations. Then, we outlined the process followed to find the optimal geometry through engineering the dispersion and, in consequence, the phase matching condition for the two main modes in the optical waveguide to attain SFWM with wide spectrally separated photons. This was achieved by analyzing the contour plots of the phase-matching condition by using straight lines that allow to delimit and find the geometry through a graphical solution.

Furthermore, we analyzed the JSI for the two-photon quantum state and found the optimal radius ($R = 155.255 \mu\text{m}$) that maximizes the overlap between the JSI in the cavity absence and the cavity functions. Finally, we found the Q-factor required to achieve the bandwidth of the photons to match the atomic transition of the Pr^{3+} ions.

We want to emphasize that this is possible because Si_3N_4 is a material with a relatively high refractive index, though not as high as other materials (such as

5. CONCLUSIONS

SOI, AlGaAs, etc.), which enables the design of photonic circuits compatible with both visible and infrared wavelengths.

- An integrated photon source engineered to produce a broadband spectrum.

Similarly to the previous description, we performed our analysis to find the geometrical parameters of an integrated photon source based on a microring resonator. In this case, the main goal was to achieve a bright broadband quantum frequency comb at telecom wavelengths.

We started our analysis by examining the dispersion profile for two structures with different top air cladding: SiO₂ and air, for fixed height of 500 nm and several widths. The waveguides with the SiO₂ cladding do not achieve anomalous dispersion at 1550 nm, while the waveguides with the air cladding can achieve low anomalous dispersion at 1550 nm by properly changing the width of the ridge waveguide. After finding that the use of air cladded waveguides is suitable for achieving anomalous dispersion, we compared with recently reported waveguides with a thickness of 800 nm and SiO₂ cladding. We found that our photon source can achieve a broadband spectrum in comparison with the thick waveguides. Then, we estimated the theoretical photon flux for both sources, in which our proposed photon source predicts as well a higher number of photons.

Finally, we characterized our microring resonators classically and compared the results with the theoretical values. The theoretical estimated parameters, such as FSR and integrated dispersion, are in good agreement with the measurements. The theoretical FSR for the TE₀₀ and TM₀₀ modes are 50.2 GHz and 50.6 GHz, respectively, while the average measured values are 51 GHz and 51.8 GHz for the TE₀₀ and TM₀₀ modes. We consider this an excellent indicator of the performance of our source with less than 1 GHz difference which is attributed to fabrication errors. Moreover, we measured the bandwidth of the resonances and in consequence, the quality factors. These Q-factors are in the order of $Q \approx 10^4$ which indicates high losses in the microring. This is mainly attributed to the fabrication process which should be improved. In addition, the temperature shifting of the resonances was characterized for a short range of scanned temperatures, showing these devices as candidates for alternative applications such as integrated sensors.

As a final conclusion, integrated photonic circuits, designed, fabricated and characterized during this PhD thesis, constitute the first integrated photon sources fabricated and characterized within the framework of an international collaboration between CIO in Mexico, UTT in France and LUH in Germany. This collaborations can allow a great impact in technology development in Mexico.

5.1 Perspectives

The following points are of interest for the development of future devices.

- Improvement in the fabrication process to achieve higher Q-factor and low propagation losses.
- Alternative designs such as cascaded microring resonators or coupled Fabry-Perot cavities that allow to achieve higher Q-factors without sacrificing the photon flux.
- Design, engineering and implementation of integrated photon sources at visible wavelengths due to the high compatibility of Si_3N_4 at visible-telecom wavelengths.
- Implementation of the design process used in this thesis to novel materials with interesting properties such as high nonlinear refractive index for brighter photon sources.
- Research of hybrid SiO_2 -air cladding devices for optimal coupling as well as applications in photonic quantum technologies.

List of Publications

Published articles

LA Tapia-Licona, **JSS Durán-Gómez**, EG Trejo-Liévano, GV Vázquez, R Ramírez-Alarcón, ME Soto-Alcaraz, and R Castro-Beltrán. Design and fabrication of Mach-Zehnder interferometers in soda-lime glass for temperature sensing applications. *Applied Optics*, 62(5):1214-1220, 2023.

Alí M Angulo, Jan Heine, **JSS Durán-Gómez**, Hatam Mahmudlu, Raktim Haldar, Charalambos Klitis, Marc Sorel and Michael Kues. Shaping the spectral correlation of bi-photon quantum frequency combs by multi-frequency excitation of an SOI integrated nonlinear resonator. *Optics Letters*, 48(21):5583–5586, 2023.

JSS Durán-Gómez, R Ramírez-Alarcón, M Gómez Robles, PMC Tavares Ramírez, GJ Rodríguez Becerra, E Ortíz-Ricardo and R Salas-Montiel. Integrated photon pair source based on a silicon nitride micro-ring resonator for quantum memories. *Optics Letters*, 49(7) : 1860–1863, 2024.

PMC Tavares Ramírez, **JSS Durán-Gómez**, GJ Rodríguez Becerra, R Ramírez-Alarcón, M Gómez Robles and R Salas-Montiel. Integrated photon pairs source in silicon carbide based on micro-ring resonators for quantum storage at telecom wavelengths. *Scientific Reports*, 14(1):17755, 2024.

GJ Rodríguez Becerra, **JSS Durán-Gómez**, PMC Tavares Ramírez, R Ramírez-Alarcón, M Gómez Robles and R Salas-Montiel. Integrated photon pair source based on counter-propagating spontaneous four wave mixing in a silicon nitride microring resonator. *Applied Optics*, 63(27):7278–7285, 2024.

Dante Urbietta-Maldonado, **JSS Durán-Gómez**, Roberto Ramírez Alarcón and Laura E. C. Rosales-Zárate. Dynamics of a Schrödinger cat state in a photonic waveguides array. *Accepted in JOSA-B*, December 2024.

Bibliography

- [1] Thaddeus D Ladd, Fedor Jelezko, Raymond Laflamme, Yasunobu Nakamura, Christopher Monroe, and Jeremy Lloyd O’Brien. Quantum computers. *nature*, 464(7285):45, 2010. [1](#)
- [2] Fulvio Flamini, Nicolo Spagnolo, and Fabio Sciarrino. Photonic quantum information processing: a review. *Reports on Progress in Physics*, 82(1):016001, 2018. [1](#)
- [3] Fulvio Flamini, Lorenzo Magrini, Adil S Rab, Nicolò Spagnolo, Vincenzo D’ambrosio, Paolo Mataloni, Fabio Sciarrino, Tommaso Zandrini, Andrea Crespi, Roberta Ramponi, et al. Thermally reconfigurable quantum photonic circuits at telecom wavelength by femtosecond laser micromachining. *Light: Science & Applications*, 4(11):e354, 2015. [1](#), [2](#)
- [4] Andrea Crespi, Mirko Lobino, Jonathan CF Matthews, Alberto Politi, Chris R Neal, Roberta Ramponi, Roberto Osellame, and Jeremy L O’Brien. Measuring protein concentration with entangled photons. *Applied Physics Letters*, 100(23):233704, 2012. [1](#)
- [5] Simeon Bogdanov, MY Shalaginov, Alexandra Boltasseva, and Vladimir M Shalaev. Material platforms for integrated quantum photonics. *Optical Materials Express*, 7(1):111–132, 2017. [1](#), [2](#)
- [6] Jonathan P Dowling and Kaushik P Seshadreesan. Quantum optical technologies for metrology, sensing, and imaging. *Journal of Lightwave Technology*, 33(12):2359–2370, 2015. [1](#)
- [7] Michael Kues, Christian Reimer, Piotr Roztocki, Luis Romero Cortés, Stefania Sciara, Benjamin Wetzal, Yanbing Zhang, Alfonso Cino, Sai T Chu, Brent E Little, et al. On-chip generation of high-dimensional entangled quantum states and their coherent control. *Nature*, 546(7660):622–626, 2017. [1](#), [12](#)
- [8] Jeremy L O’Brien, Akira Furusawa, and Jelena Vučković. Photonic quantum technologies. *Nature Photonics*, 3(12):687, 2009. [1](#)
- [9] Jianwei Wang, Fabio Sciarrino, Anthony Laing, and Mark G Thompson. Integrated photonic quantum technologies. *Nature Photonics*, 14(5):273–284, 2020. [1](#), [2](#)

BIBLIOGRAPHY

- [10] Taira Giordani, Francesco Hoch, Gonzalo Carvacho, Nicolò Spagnolo, and Fabio Sciarrino. Integrated photonics in quantum technologies. *La Rivista del Nuovo Cimento*, 46(2):71–103, 2023. [1](#)
- [11] Laurent Labonté, Olivier Alibart, Virginia D’Auria, Florent Doutre, Jean Etesse, Gregory Sauder, Anthony Martin, Éric Picholle, and Sébastien Tanzilli. Integrated photonics for quantum communications and metrology. *PRX Quantum*, 5(1):010101, 2024. [1](#), [2](#)
- [12] Emanuele Pelucchi, Giorgos Fagas, Igor Aharonovich, Dirk Englund, Eden Figueroa, Qihuang Gong, Hübel Hannes, Jin Liu, Chao-Yang Lu, Nobuyuki Matsuda, et al. The potential and global outlook of integrated photonics for quantum technologies. *Nature Reviews Physics*, 4(3):194–208, 2022. [1](#), [2](#)
- [13] Galan Moody, Lin Chang, Trevor J Steiner, and John E Bowers. Chip-scale nonlinear photonics for quantum light generation. *AVS Quantum Science*, 2(4), 2020. [1](#), [12](#)
- [14] Galan Moody, Volker J Sorger, Daniel J Blumenthal, Paul W Juodawlkis, William Loh, Cheryl Sorace-Agaskar, Alex E Jones, Krishna C Balram, Jonathan CF Matthews, Anthony Laing, et al. 2022 roadmap on integrated quantum photonics. *Journal of Physics: Photonics*, 4(1):012501, 2022. [1](#), [2](#)
- [15] Haoyang Wang, Qiang Zeng, Haiqiang Ma, and Zhiliang Yuan. Progress on chip-based spontaneous four-wave mixing quantum light sources. *Advanced Devices & Instrumentation*, 5:0032, 2024. [1](#), [2](#), [33](#)
- [16] M Davanco, L Chang, JE Bowers, N Quack, C Galland, I Aharonovich, MA Wolff, C Schuck, N Sinclair, M Loncar, et al. Roadmap on integrated quantum photonics. *J. Phys. Photonics*, 4(1):012501, 2022. [1](#), [2](#)
- [17] Liao Duan, Trevor J Steiner, Paolo Pintus, Lillian Thiel, Joshua E Castro, John E Bowers, and Galan Moody. Broadband entangled-photon pair generation with integrated photonics: Guidelines and a materials comparison. *arXiv preprint arXiv:2407.04792*, 2024. [2](#), [33](#)
- [18] K. M. Davis, K. Miura, N. Sugimoto, and K. Hirao. Writing waveguides in glass with a femtosecond laser. *Optics Letters*, 21:1729–1731, 1996. [2](#)
- [19] Huan Huang, Lih Mei Yang, and Jian Liu. Femtosecond fiber laser direct writing of optical waveguide in glasses. *SPIE*, 81640B, 2011. [2](#)
- [20] C Vieu, F Carcenac, A Pepin, Y Chen, M Mejias, A Lebib, L Manin-Ferlazzo, L Couraud, and H Launois. Electron beam lithography: resolution limits and applications. *Applied surface science*, 164(1-4):111–117, 2000. [2](#)
- [21] M Bruel. Silicon on insulator material technology. *Electronics letters*, 31(14):1201–1202, 1995. [2](#)

- [22] Joshua W Silverstone, Damien Bonneau, Jeremy L O'Brien, and Mark G Thompson. Silicon quantum photonics. *IEEE Journal of Selected Topics in Quantum Electronics*, 22(6):390–402, 2016. [2](#)
- [23] Jianwei Wang, Stefano Paesani, Yunhong Ding, Raffaele Santagati, Paul Skrzypczyk, Alexia Salavrakos, Jordi Tura, Remigiusz Augusiak, Laura Mančinska, Davide Bacco, et al. Multidimensional quantum entanglement with large-scale integrated optics. *Science*, 360(6386):285–291, 2018. [2](#)
- [24] Juan Samuel S Durán Gómez. Integrated nanophotonic waveguide lattices as photonic quantum simulators. Master's thesis, Centro de Investigaciones en Óptica A.C., 2019. [2](#), [20](#), [45](#)
- [25] JM Chavez Boggio, D Bodenmüller, T Fremberg, R Haynes, MM Roth, R Eisermann, M Lisker, L Zimmermann, and M Böhm. Dispersion engineered silicon nitride waveguides by geometrical and refractive-index optimization. *JOSA B*, 31(11):2846–2857, 2014. [2](#), [9](#), [33](#)
- [26] Katsunari Okamoto. *Fundamentals of Optical Waveguides*. Academic Press, 2006. [5](#), [6](#), [9](#)
- [27] Ginés Lifante. *Integrated Photonics: Fundamentals*. Wiley, 2003. [5](#), [6](#)
- [28] John. D. Joannopoulos, Steven G. Johnson, Joshua N. Winn, and Robert D. Meade. *Photonic crystals: molding the flow of light*. Princeton University press, 2008. [7](#)
- [29] O. V. Ivanova, M. Hammer, R. Stoffer, and E. van Groesen. A variational mode expansion mode solver. *Optical and Quantum Electronics*, 39(10):849–864, 2007. [8](#)
- [30] Govind P Agrawal. Nonlinear fiber optics. In *Nonlinear Science at the Dawn of the 21st Century*, pages 195–211. Springer, 2000. [9](#), [12](#)
- [31] John Heebner, Rohit Grover, and Tarek Ibrahim. *Optical microresonator theory*. Springer, 2008. [9](#), [10](#)
- [32] Shun Fujii and Takasumi Tanabe. Dispersion engineering and measurement of whispering gallery mode microresonator for kerr frequency comb generation. *Nanophotonics*, 9(5):1087–1104, 2023-03-30 2020. [11](#), [25](#)
- [33] Victor Brasch, Michael Geiselmann, Tobias Herr, Grigoriy Lihachev, Martin HP Pfeiffer, Michael L Gorodetsky, and Tobias J Kippenberg. Photonic chip-based optical frequency comb using soliton cherenkov radiation. *Science*, 351(6271):357–360, 2016. [11](#), [12](#)

BIBLIOGRAPHY

- [34] Shun Fujii, Shuya Tanaka, Mika Fuchida, Hikaru Amano, Yuka Hayama, Ryo Suzuki, Yasuhiro Kakinuma, and Takasumi Tanabe. Octave-wide phase-matched four-wave mixing in dispersion-engineered crystalline microresonators. *Optics letters*, 44(12):3146–3149, 2019. [12](#)
- [35] Robert W Boyd, Alexander L Gaeta, and Enno Giese. Nonlinear optics. In *Springer Handbook of Atomic, Molecular, and Optical Physics*, pages 1097–1110. Springer, 2018. [12](#)
- [36] Jorge Monroy-Ruz, Karina Garay-Palmett, and Alfred B U'Ren. Counter-propagating spontaneous four wave mixing: photon-pair factorability and ultra-narrowband single photons. *New Journal of Physics*, 18(10):103026, 2016. [12](#)
- [37] Christian Reimer, Michael Kues, Lucia Caspani, Benjamin Wetzal, Piotr Roztockii, Matteo Clerici, Yoann Jestin, Marcello Ferrera, Marco Peccianti, Alessia Pasquazi, et al. Cross-polarized photon-pair generation and bi-chromatically pumped optical parametric oscillation on a chip. *Nature Communications*, 6(1):1–7, 2015. [12](#)
- [38] Brian J Smith, P Mahou, Offir Cohen, JS Lundeen, and IA Walmsley. Photon pair generation in birefringent optical fibers. *Optics express*, 17(26):23589–23602, 2009. [13](#)
- [39] K Garay-Palmett, Y Jeronimo-Moreno, and A B U'Ren. Theory of cavity-enhanced spontaneous four wave mixing. *Laser Physics*, 23(1):015201, 2013. [13](#), [14](#), [15](#)
- [40] Karina Garay-Palmett, Dong Beom Kim, Yujie Zhang, Francisco A Domínguez-Serna, Virginia O Lorenz, and Alfred B U'Ren. Fiber-based photon-pair generation: tutorial. *JOSA B*, 40(3):469–490, 2023. [14](#)
- [41] Erasto Ortiz-Ricardo, Cesar Bertoni-Ocampo, Mónica Maldonado-Terrón, Arturo Garcia Zurita, Roberto Ramirez-Alarcon, Hector Cruz Ramirez, Rigoberto Castro-Beltrán, and Alfred B U'Ren. Submegahertz spectral width photon pair source based on fused silica microspheres. *Photonics Research*, 9(11):2237–2252, 2021. [15](#)
- [42] Jelena V Rakonjac, Samuele Grandi, Sören Wengerowsky, Dario Lago-Rivera, Félicien Appas, and Hugues de Riedmatten. Transmission of light-matter entanglement over a metropolitan network. *Optica Quantum*, 1(2):94–102, 2023. [17](#)
- [43] L Ma, O Slattery, and X Tang. Optical quantum memory and its applications in quantum communication systems. *J. Res. Natl. Inst. Stan.*, 125(125002):1–13, 2020. [17](#)
- [44] Jelena V Rakonjac, Giacomo Corrielli, Dario Lago-Rivera, Alessandro Seri, Margherita Mazzera, Samuele Grandi, Roberto Osellame, and Hugues de Riedmatten. Storage and analysis of light-matter entanglement in a fiber-integrated system. *Science Advances*, 8(27):eabn3919, 2022. [17](#)

- [45] Jianji Liu, Jiachen Liu, Ping Yu, and Guoquan Zhang. Sub-megahertz narrow-band photon pairs at 606 nm for solid-state quantum memories. *APL Photonics*, 5(6):066105, 2020. [17](#)
- [46] JSS Durán Gómez, R Ramírez Alarcón, M Gómez Robles, PMC Tavares Ramírez, GJ Rodríguez Becerra, and E Ortíz-Ricardo. Integrated photon pair source based on a silicon nitride micro-ring resonator for quantum memories. *Optics Letters*, 49(7):1860–1863, 2024. [17](#)
- [47] M Nicolle, JN Becker, C Weinzetl, IA Walmsley, and PM Ledingham. Gigahertz-bandwidth optical memory in pr 3+: Y 2 sio 5. *Optics Letters*, 46(12):2948–2951, 2021. [17](#)
- [48] Jelena V Rakonjac, Dario Lago-Rivera, Alessandro Seri, Margherita Mazzera, Samuele Grandi, and Hugues de Riedmatten. Entanglement between a telecom photon and an on-demand multimode solid-state quantum memory. *Physical Review Letters*, 127(21):210502, 2021. [17](#)
- [49] Mateus Corato-Zanarella, Xingchen Ji, Aseema Mohanty, and Michal Lipson. Absorption and scattering limits of silicon nitride integrated photonics in the visible spectrum. *Optics Express*, 32(4):5718–5728, 2024. [17](#)
- [50] Mateus Corato-Zanarella, Andres Gil-Molina, Xingchen Ji, Min Chul Shin, Aseema Mohanty, and Michal Lipson. Widely tunable and narrow-linewidth chip-scale lasers from near-ultraviolet to near-infrared wavelengths. *Nature Photonics*, 17(2):157–164, 2023. [17](#)
- [51] Yi Sun, Jordan Stone, Xiyuan Lu, Feng Zhou, Junyeob Song, Zhimin Shi, and Kartik Srinivasan. Advancing on-chip kerr optical parametric oscillation towards coherent applications covering the green gap. *Light: Science & Applications*, 13(1):201, 2024. [17](#)
- [52] GJ Rodríguez Becerra, JSS Durán Gómez, PMC Tavares Ramírez, R Ramírez Alarcón, M Gómez Robles, and R Salas-Montiel. Integrated photon pairs source based on counter-propagating spontaneous four wave mixing in a silicon nitride microring resonator. *Applied Optics*, 63(27):7278–7285, 2024. [17](#)
- [53] <https://www.fs.com/products/126903.html?attribute=29245&id=1565142>. [19](#)
- [54] Vortex Tunable Lasers. Newport. <https://www.newport.com/p/TLB-6817>. [20](#)
- [55] Kevin Luke, Yoshitomo Okawachi, Michael RE Lamont, Alexander L Gaeta, and Michal Lipson. Broadband mid-infrared frequency comb generation in a si 3 n 4 microresonator. *Optics letters*, 40(21):4823–4826, 2015. [20](#)

BIBLIOGRAPHY

- [56] Ian H Malitson. Interspecimen comparison of the refractive index of fused silica. *Josa*, 55(10):1205–1209, 1965. 20
- [57] ID Quantique. ID230. <https://www.idquantique.com/quantum-detection-systems/products/id230/>. 24
- [58] Muhammad A Butt, Lukasz Kozłowski, Michał Golas, Mateusz Slowikowski, Maciej Filipiak, Marcin Juchniewicz, Aleksandra Bieniek-Kaczorek, Michał Dudek, and Ryszard Piramidowicz. Numerical and experimental demonstration of a silicon nitride-based ring resonator structure for refractive index sensing. *Applied Sciences*, 14(14):6082, 2024. 33
- [59] T Melton, JF McMillan, J Yang, W Wang, Y Lai, M Gerber, M Rodriguez, JP Hubschman, K Nouri-Mahdavi, and CW Wong. Optical coherence tomography imaging and noise characterization based on 1- μ m microresonator frequency combs. *APL Photonics*, 9(8), 2024. 33
- [60] Zhen-Sheng Yuan, Xiao-Hui Bao, Chao-Yang Lu, Jun Zhang, Cheng-Zhi Peng, and Jian-Wei Pan. Entangled photons and quantum communication. *Physics Reports*, 497(1):1–40, 2010. 33
- [61] Hsuan-Hao Lu, Joseph M Lukens, Nicholas A Peters, Brian P Williams, Andrew M Weiner, and Pavel Lougovski. Quantum interference and correlation control of frequency-bin qubits. *Optica*, 5(11):1455–1460, 2018. 33
- [62] Alán Aspuru-Guzik and Philip Walther. Photonic quantum simulators. *Nature Physics*, 8:285 EP –, 04 2012. 33
- [63] Anamika Nair Karunakaran, Marco Clementi, Christian Lafforgue, Ozan Yakar, Anton Stroganov, Poul Varming, Minhao Pu, Kresten Yvind, Patrick Montague, and Camille-Sophie Brès. Dissipative kerr soliton generation at 2 μ m in a silicon nitride microresonator. *Optics Express*, 32(9):14929–14939, 2024. 33, 36
- [64] Yi Sun, Jordan Stone, Xiyuan Lu, Feng Zhou, Junyeob Song, Zhimin Shi, and Kartik Srinivasan. Advancing on-chip kerr optical parametric oscillation towards coherent applications covering the green gap. *Light: Science & Applications*, 13(1):201, 2024. 33
- [65] Yaping Hong, Yixiao Hong, Jianxun Hong, and Guo-Wei Lu. Dispersion optimization of silicon nitride waveguides for efficient four-wave mixing. In *Photonics*, volume 8, page 161. MDPI, 2021. 33
- [66] K Sugiura, Z Yin, R Okamoto, L Zhang, L Kang, J Chen, P Wu, ST Chu, BE Little, and S Takeuchi. Broadband generation of photon-pairs from a cmos compatible device. *Applied Physics Letters*, 116(22), 2020. 33

- [67] Ryota Wakabayashi, Mikio Fujiwara, Ken-ichiro Yoshino, Yoshihiro Nambu, Masahide Sasaki, and Takao Aoki. Time-bin entangled photon pair generation from a micro-ring resonator. *Optics express*, 23(2):1103–1113, 2015. [33](#)
- [68] Alexander Miloshevsky, Lucas M Cohen, Karthik V Myilswamy, Muneer Al-showkan, Saleha Fatema, Hsuan-Hao Lu, Andrew M Weiner, and Joseph M Lukens. Cmos photonic integrated source of broadband polarization-entangled photons. *Optica Quantum*, 2(4):254–259, 2024. [33](#)
- [69] Trevor J Steiner, Maximilian Shen, Joshua E Castro, John E Bowers, and Galan Moody. Continuous entanglement distribution from an all-glass-on-insulator micro-comb for quantum communications. *Optica Quantum*, 1(2):55–62, 2023. [33](#)
- [70] Hong Zeng, Zhao-Qin He, Yun-Ru Fan, Yue Luo, Chen Lyu, Jin-Peng Wu, Yun-Bo Li, Sheng Liu, Dong Wang, De-Chao Zhang, et al. Quantum light generation based on a silicon microring toward a fully on-chip source. *Physical Review Letters*, 132(13):133603, 2024. [33](#)
- [71] Hiep X Dinh, Armandas Balčytis, Tomoki Ozawa, Yasutomo Ota, Guanghui Ren, Toshihiko Baba, Satoshi Iwamoto, Arnan Mitchell, and Thach G Nguyen. Reconfigurable synthetic dimension frequency lattices in an integrated lithium niobate ring cavity. *Communications Physics*, 7(1):185, 2024. [33](#)
- [72] Zhenghao Yin, Kenta Sugiura, Hideaki Takashima, Ryo Okamoto, Feng Qiu, Shiyoshi Yokoyama, and Shigeki Takeuchi. Frequency correlated photon generation at telecom band using silicon nitride ring cavities. *Optics Express*, 29(4):4821–4829, 2021. [33](#), [36](#)
- [73] Wenjun Wen, Wenhan Yan, Chi Lu, Liangliang Lu, Xiaoyu Wu, Yanqing Lu, Shining Zhu, and Xiao-Song Ma. Polarization-entangled quantum frequency comb from a silicon nitride microring resonator. *Physical Review Applied*, 20(6):064032, 2023. [33](#), [36](#)
- [74] Gregory Moille, Daron Westly, and Kartik Srinivasan. Broadband visible wavelength microcomb generation in silicon nitride microrings through air-clad dispersion engineering. *arXiv preprint arXiv:2404.01577*, 2024. [33](#)
- [75] Helge Gehring, Matthias Blaicher, Wladick Hartmann, and Wolfram HP Pernice. Python based open source design framework for integrated nanophotonic and superconducting circuitry with 2d-3d-hybrid integration. *OSA Continuum*, 2(11):3091–3101, 2019. [46](#)